Temporal mapping of photochemical reactions and molecular excited states with carbon specificity

K. Wang[1,2,‡], P. Murahari[2,‡], K. Yokoyama[2,3], J. S. Lord[3], F. L. Pratt[3], J. He[1], L Schulz[1], M Willis[1], J. E. Anthony[4], N. A. Morley[5], L. Nuccio[6], A. Misquitta[2], D. J. Dunstan[2], K. Shimomura[7], I. Watanabe[8], S Zhang[1], P. Heathcote[9,*], A. J. Drew[1,2,3,*]

[1] College of Physical Sciences and Technology, Sichuan University, Chengdu, Sichuan, 610064 P. R. China

[2] School of Physics and Astronomy, Queen Mary University of London, Mile End, London, E1 4NS, UK

[3] ISIS Muon Facility, Rutherford Appleton Laboratory, Didcot, OX11 0QX, UK

[4] Department of Chemistry, University of Kentucky, Lexington, Kentucky 40506, USA

[5] Department of Materials Science and Engineering, University of Sheffield, Sheffield, S1 3JD, UK

[6] University of Fribourg, Department of Physics and Fribourg Centre for Nanomaterials, Chemin du Musée 3, CH-1700 Fribourg, Switzerland

[7] Materials and Life Science Division, J-PARC Center, Tokai, Ibaraki 319-1195, Japan

[8] RIKEN-RAL, Nishina Centre, 2-1 Hirosawa, Wako, Saitama, 351-0198, Japan

[9] School of Biological and Chemical Sciences, Queen Mary University of London, Mile End, London, E1 4NS, UK

‡ These authors contributed equally to this work.

*Correspondence to: A.J.Drew@qmul.ac.uk or P.Heathcote@qmul.ac.uk

Photochemical reactions are essential to a large number of important industrial and biological processes. A method for monitoring photochemical reaction kinetics and the dynamics of molecular excitations with spatial resolution within the active molecule would allow a rigorous exploration of the pathway and mechanism of photophysical and photochemical processes. Here we demonstrate that laser-excited muon pump-probe spin spectroscopy (photo-μSR) can temporally and spatially map these processes with a spatial resolution at the single-carbon level in a molecule with a pentacene backbone. The observed time-dependent light-induced changes of an avoided level crossing resonance demonstrate that the photochemical reactivity of a specific carbon atom is modified as a result of the presence of the excited state wavefunction. This demonstrates the sensitivity and potential of this technique in probing molecular excitations and photochemistry.

Dynamics of molecular excited states govern photochemical reactions that are key to a phenomenal number of important industrial and biological processes. For example, molecules in living organisms are often exposed to solar radiation, and in the case of photosynthesis this light energy is captured to provide the energy that supports almost all life. Moreover, the effect of this solar radiation on biomolecules such as DNA plays an important evolutionary role[1,2]. In the chemical engineering field, stereoselective synthesis enables the construction of a vast array of organic molecules with precise control over their three-dimensional structure[3,4], which is important in a variety of fields ranging from drug discovery to materials engineering. Photochemical reactions have a substantial impact on these fields by affording direct access to certain structural motifs that are otherwise difficult to construct[5]. For example, the malaria drug artemisinin is commercially produced with a key photochemical step[6]. In organic electronics the complex physics of excitations is critical to device function[7-13]. High efficiencies have been reached for both organic light emitting diodes (OLEDs) and organic photovoltaics (OPVs)[14-17], yet a major barrier to the deployment of organic semiconductors is their functional lifetime[17]. For example, a recent study of the chemical reactivity of derivatives of anthracene and tetracene in the OLED environment indicates that free-radical chemistry is initiated after photo-excitation by homolytic bond dissociation reactions, which result in hydrogenation reactions[18].

We have developed the experimental technique photo-μSR[19] so that it can now measure the spatial distribution of electron density in the molecular excited state at any given time. Whilst this technique has previously been used to study excitations predominantly in semiconductors[19,20] and a limited number of solutions of organic molecules[21], no spatial information has been gained up until now. By making use of Avoided Level Crossing (ALC) spectroscopy, whose resonance positions are specific to individual carbons, we demonstrate that crucial information on the fundamental photochemical and excited state processes can be obtained. We demonstrate this new application of the technique in a 10 mM solution of the organic semiconductor 6,13-bis(tri(isopropyl)silylethynyl) pentacene (TIPS-Pn) (Figure 1a), dissolved in O_2-free dichloromethane (DCM). We present convincing evidence that muonium is able to map the time evolution of the excited state wavefunction on the pentacene backbone of the molecule, as a direct result of its sensitivity to electron density when reacting. We demonstrate that reaction of muonium with this extended aromatic system probes the relative levels of chemical reactivity of carbon atoms after excitation with light, and that this can be tracked as a function of time.

Photo-μSR

In our photo-μSR experiment, a 25 Hz, ~10 ns pulsed Nd:YAG laser was used to excite the TIPS-Pn molecules in solution with a wavelength of 532 nm and a pulse energy of 91 mJ. The light-pump muon-probe measurements were carried out on the HiFi spectrometer at the ISIS pulsed muon source, with the light flash triggered to arrive T_L before the muon pulse, to excite the TIPS-Pn molecules prior to the arrival of the muons, as depicted in Figures 1b and c. The changes to the photochemical reaction rates as a result of the excitation can then be probed with muonium, a chemical analogue of hydrogen (see below). The 25 Hz laser in combination with the 50 Hz muon pulse enabled light on/off data to be gated to alternate histograms, thus averaging out any long-term changes to the sample and accelerator profile. Further technical details can be found elsewhere[19,22], in the Methods section and in the Supplementary Information (SI).

When implanted into many materials including organic solvents, the positively charged muons can either thermalize as diamagnetic species or form hydrogen-like muonium atoms, Mu[22]. Mu is thought of as a light pseudo-isotope of the hydrogen atom, in which an electron orbits a muon (μ^+) nucleus, which is 0.11 the mass of H and behaves chemically like an H atom[22-26]. Due to the unsaturated bonds and aromatic rings that are present, muonium can react with TIPS-Pn with almost identical chemistry to a hydrogen atom creating an electrically neutral radical. There are three species of muon in our sample, a diamagnetic and two types of paramagnetic species: the unbound solvated species with a hyperfine coupling (HFC) constant of order 4.4 GHz, and a number of muoniated radicals, which have a significantly lower HFC constant for the muon and other nuclei in the molecule that are dependent on their local environment.

Indeed, it is these differences in HFCs that depend on the muon's local environment which give us spatial sensitivity. The unpaired electron wavefunction in a radical overlaps with the nuclei and gives a series of hyperfine coupling constants for all the nuclei with non-zero spin, which are generally much lower than for the individual free atoms. In the simpler case of gases, liquids or solutions only the isotropic parts of the coupling constants need be considered. When a magnetic field is applied parallel to the muon's initial spin polarisation, the spin energy levels are split by the Zeeman interaction. At certain fields, the combination of Zeeman and hyperfine interactions cause cross-relaxation between the muon and one of the other nuclei, and a so-called avoided level crossing (ALC) resonance.[22,27,28,29]

These resonances are usually plotted as the "integral asymmetry" - the average muon polarisation weighted by the muon lifetime, and take the form of relatively sharp dips. The amplitude of the integral ALC resonance depends on the hyperfine coupling of both muon and nucleus. In many aromatic molecules each radical species has one dominant resonance due to the α-proton. The amplitude and width are also affected by relaxation and other dynamics, and the formation rate and probability of that species. ALCs from different radical species caused by different addition sites of the muonium will generally be at quite different fields, so they can be measured individually. Importantly, one of the main drivers of the relative amplitude of the various ALC resonances is the reaction kinetics associated with muonium bonding. That is itself driven by the electrostatic potential, which of course can be quite different when the molecule is in the ground state compared to an excited state. We show that our photo-μSR experiment can spatially probe the molecular excited state and its role in determining reactivity of the molecule, all at an individual atom level. Moreover, by changing the pump-probe delay time, T_L, temporal information is obtained as the transient excited species evolves with time.

Light induced effects on ALC spectra

Figure 2a shows the ALC spectra taken for muonium bound to carbons 1, 2 and 4 in TIPS-Pn at T_L = 130 ns. The laser and muon pulse are sufficiently separated to ensure that photo-ionisation of muonium or muoniated radicals could not occur[30]. Figure 2b shows the ALC from muon-electron and muon-proton (α- proton) HFCs predicted from ab-initio density functional theory (DFT) calculations, which can be used to assign the bonding site for each ALC resonance. The site assignment is in the inset. Further details of these DFT calculations can be found in the SI. It is immediately clear that photo-excited changes to the spectra are evident for sites 1 and 2 but not site 4. The largest changes are evident at site 2, with a clear increase in amplitude, or area of the ALC, as well as a small shift in the ALC minima (potentially as a result of a HFC change). There could be an increase in the width of the lines for both sites 1 and 2, although this is

difficult to quantify since these ALCs overlap. Figure 2c inset shows the light-induced change in asymmetry, A_{diff}, as a function of T_L, at two fixed fields (indicated by the arrows in Figure 2a), corresponding to sites 2 and 4 (indicated by the arrows in Figure 1a). There are two components present corresponding to ALC spectral changes at site 2, with different signs and timescales, that are not present at site 4. The 6.5 μs lifetime of the triplet molecular excited state is clearly evident in the slower component - strong evidence that muonium is directly detecting the presence of triplet excited states. The ALC amplitude of this component is reduced in the triplet state. The faster component, with an increased ALC amplitude, has a timescale of approximately 1 μs.

Light-induced changes to the ALC spectra can take many forms, for example additional resonances could appear or ALC positions could shift, due to the presence of a distribution of unpaired spin on the molecule[19]. There could be a change in hyperfine coupling constant due to a structural or conformational difference[31], an increased electron spin relaxation or exchange[32-34], or a modification of the muonium reaction rate for a given carbon[31]. It is extremely unlikely that a conformational change or unpaired spin can account for this data, as the ALC at around 300 mT for site 4 is identical for the light on and off cases. Either conformational or unpaired spin changes would modify the muon-electron and/or proton-electron isotropic hyperfine coupling (HFC) for all adducts[31]. For the same reasons, we also discount localized heating as a result of absorption of the light, since a relatively small change in temperature is known to significantly alter the position of the ALC for site 4 (see Figure S4 in the SI). We also believe that electron spin relaxation and/or spin exchange cannot account for these changes, as it is known to affect all ALCs in a similar fashion in the solid state[32,33], there is no associated increase in relaxation rate and it cannot account for all of the features in the time dependent data (see the SI). To explain our observations, one must invoke the mechanism of radical formation from the solvated muonium. Muons thermalize very quickly, in less than 1 ns,[22] with the final result in fully saturated organic solvents being a mixture of solvated muonium and unresolved diamagnetic muon states. The muonium then chemically reacts with the unsaturated or aromatic solute molecules, and if this final stage is not sufficiently prompt, then a number of features are observed in the data, which evolve with the reaction rate. These features, discussed below, are not present in the other candidate mechanisms mentioned above.

Interpreting the ALC spectra

In a weak transverse field (WTF), the energy difference between the two triplet transitions $|m_\mu,m_e\rangle = |½,½\rangle \rightarrow (|½,-½\rangle + |-½,½\rangle)/\sqrt{2}$ and $(|½,-½\rangle + |-½,½\rangle)/\sqrt{2} \rightarrow |-½,-½\rangle$ are equal and relatively small, resulting in low-frequency Rabi oscillations[22,27]. The WTF spectra shown in Figure 3a and b, demonstrate a clear triplet precession signal (fast oscillation) superimposed on the precession from the diamagnetic muons (slow oscillation). The triplet precession results from muonium that stop in the unbound state, either in the SiO_2 window or the solvent. For muoniated radicals, the magnetic field at which the Zeeman splitting becomes non-linear (i.e the two triplet transitions have a different energy) is significantly lower and the proton coupling splits the triplet energy difference. Given there are multiple radical states with different muon-electron and proton-electron HFC, the resulting signal is rather more complex, comprising of a superposition of multiple beating signals. We note that this will be also true for muonium addition to the triple bond of the sidegroup, despite it not having an α-proton (see SI). Moreover, the larger dynamics present in bound muonium and the nuclear HFC significantly relaxes the triplet precession. All of these effects conspire together to make the radical triplet precession signal in a WTF all but

invisible. However, changes in the solvated muonium amplitude, present if there is a light induced change in reaction rate, are readily observable in the data upon fitting the spectra to $A(t) = A_{mu}\cos(\omega_{mu}t+\phi_{mu})\exp(-(\sigma_{mu}t)^2) + A_{\mu^+}\cos(\omega_{\mu^+}t+\phi_{\mu^+})\exp(-(\sigma_{\mu^+}t)^2)$. This represents a Gaussian damped precession of the triplet muonium (first term) and spin precession in the applied field of the diamagnetic muons (second term), from which the light induced change in the triplet precession asymmetry, $A_{WTF} = A_{mu(on)} - A_{mu(off)}$, is extracted. Figure 3c shows A_{WTF} with T_L = 130 ns, for several WTFs. All show a reduction in asymmetry of the triplet precession signal under photo-excitation, and this reduction appears to be field independent within error. This change is also present in the Fourier transforms of the data, an example of which is shown in Figure 3d (see Figure S5 in the SI for all the Fourier transforms). This is clear evidence that there is an overall reduction in the amount of solvated muonium present following photo-excitation, which is consistent with an increased reaction rate of the solvated muonium with the molecule following excitation.

This conclusion has some implications about the timescales. If the reaction rate is comparable with the solvated muonium hyperfine frequency, then the shape of the LF repolarisation curve is strongly governed by the reaction rate, as the muon partially exchanges spin polarisation with the electron before forming the radical. However, the ALC amplitude is almost reaction rate independent, since at high fields the muon's spin should be nearly or fully repolarized. Clearly, we are not in this fast regime. If, on the other hand, the inverse reaction rate approaches the lifetime of the muon (in excess of ~100 ns), then the ALC amplitude is dependent on the reaction rate, as some muons will decay and be measured before they have a chance to react. Moreover, in this slow limit, there will be a clear two-step signature in the ground-state LF repolarisation curve and only a weak light-induced effect in the intermediate field region of the LF repolarisation. Both of these features are very clear in Figure 4a and b. Importantly, the data shown in Figure 4a corresponds to a 10 mM solution of TIPS-Pn in DCM using a standard Titanium cell mounted on an Aluminium plate, on the EMU spectrometer at ISIS. Because of the materials used in this cell, the two-step repolarization curve clearly evident in Figure 4a *must* be from the TIPS-Pn or DCM, and not the surrounding environment. This is strong evidence for either an entirely unreacted fraction of muonium, or a relatively slow reaction rate of muonium with the molecule.

Bringing all of the above information together, the light induced changes to the ALC spectra in Figure 2a are mainly related to a change in the reaction rate of the muonium with the molecule, specific to carbon 2. Whilst the mechanism of photodegradation in TIPS-Pn has not been fully clarified[35, 36], it has previously been inferred that TIPS-Pn undergoes a photoinduced inter-molecular 4 + 4 cycloaddition via a π-dimerization process[35]. However, we see little evidence for the reaction rate of muonium with site 4 being enhanced by excitation, probably because muonium chemistry is a good model for radical reactions, whereas dimerization of TIPS-Pn is an electrocyclic reaction.

Quantum chemical calculations were used to explore the electrostatic potentials that promote or inhibit molecular interactions, and to identify regions of the TIPS-Pn molecule with higher chemical reactivity. DFT was used with the B3LYP functional and cc-pVDZ basis set embedded in the Gaussian package[37]. After geometry optimization, the atomic charge distribution within the molecules along with its electronic volume was determined by a population analysis of the molecular orbitals. The surface enclosing 99% of the electronic density was calculated on a grid from the molecular orbital coefficients. The molecular electrostatic potential (MEP) was

mapped[38] onto this surface (Figure 4c) for both ground state and triplet state. The potential becomes significantly less negative around the bond between carbons 1 and 2 when the triplet excited state is present, as a result of the electron density becoming more dispersed around the end ring of the backbone of the molecule. This is most easily observed by plotting the difference between the MEPs for T_1 and S_0 in the top panel of Figure 4c, which shows that there is a reduction in the electron density between carbons 1 and 2 of approximately 5%. There are also changes to the electrostatic potential in the region of carbon 4, with a clear shift of electron density towards the center of the molecule from the bond between carbons 4 and 3. The change to carbon 4 is roughly symmetrical - such that there is no large change in the overall electron density of the two bonds around carbon 4. This, coupled with steric hindrance of the side groups, may explain why there are no light-induced effects to the ALC associated with carbon 4. In addition to the changes to the electric potential governing chemical reactivity, there may also be a spin effect. It is likely that the muoniated molecule is in a doublet state, provided the spin of the muonium electron is opposite to the spin of unpaired electron already present. It is currently unknown what effect this will have on reactivity. The quartet state would result in the muon electron residing in a higher energy orbital, which would probably reduce the overall reactivity.

Molecular excited states and photochemical timescales

We now discuss the timescales presented in Figure 2c. Recently, it has been shown that triplet-triplet dimers formed in TIPS-Pn dissolved in chloroform have an emission lifetime of approximately 220 ns[39]. Whilst the 1 μs photo-μSR signal and this 220 ns dimer lifetime differ by a factor of over 4, molecular interaction probabilities are strongly dependent on both concentration and solvent, as demonstrated by work on photodegradation[36], so it is feasible that dimerisation processes are responsible for this timescale. Careful study of the transient absorption spectra reported by Walker et al.[39] for a concentration of 0.075 mol l^{-1} reveals a clear feature around 1.6 eV, also with a lifetime of approximately 1 μs. The onset of aggregate absorption in TIPS-Pn is 1.65 eV. Given this and the MEP discussed above, we suggest that the 1 μs photo-μSR component is related to an 'excimeric' process – i.e a species comprising two molecules, one in the ground state and the other in an excited state. The different electron densities of the ground state and triplet would probably promote a Coulomb initiated 'excimer' state in TIPS-Pn, which presumably then leads to the eventual 4+4 cycloaddition at carbon 4, and a net increase in the muonium reactivity at carbon 2 while this state exists. Nonetheless, further study of this transient state with a 1 μs lifetime is necessary to properly identify it and its significance.

The 6.5 μs signal matches the triplet lifetime[39] and is therefore conclusive evidence that excited state processes can be measured with muoniated radicals with intra-molecular spatial resolution. Its amplitude has the opposite sign to the 1 μs signal, suggesting that it is directly related to a reduction in the reactivity of the muonium with the molecule, as a result of the reduced electron density in the carbon 2 bonds when the molecular excited state is present, as shown by the MEPs in Fig. 4c. This result, demonstrating that the time dependence of the excited state can be probed with an intra-molecular spatial resolution, is in itself quite remarkable. In principle, it should also be possible to image the time-dependency of charge transfer states, in those systems where charge separation occurs in the excited state. Given the MEPs shown in Figure 4c, it would be interesting to probe the central carbon atoms in TIPS-Pn, but unfortunately the relevant muonium bonding sites are blocked by the steric hindrance of the side groups.

Conclusions

We have demonstrated that reaction of muonium with an extended aromatic system can probe the relative levels of susceptibility of individual carbon atoms to chemical reaction upon excitation with light, and that this can be tracked as a function of time. We have presented evidence that a possible excited state with a 1 μs lifetime could be important to the photochemical degradation of TIPS-Pn in solution. This demonstrates the use of laser pumped μSR and avoided level crossing resonances to gain insight into photochemical reactivity; clearly the technique has significant potential in other aromatic systems. We note that in TIPS-Pn, there are no polar species that would result in charge transfer states, so the changes to the electrostatic potential are relatively small. It would be interesting to extend this technique to molecules with such polar groups, where much larger changes to the electrostatic potential may be present, perhaps by either chemical modification of the TIPS-Pn backbone or by studying a known donor-acceptor molecule.

There is a second component that matches the triplet lifetime, 6.5 μs. This is strong evidence that muonium is able to map the time evolution of the excited state wavefunction on the molecule as a direct result of its sensitivity to electron density when reacting. This provides spatial resolution for studying excited state dynamics. To our knowledge, the experimental approach used here is the only one with this degree of temporal combined direct intra-molecular spatial sensitivity; for example, typical resolution in other mapping techniques are in excess of ten nm[40,41]. It may also be possible to extend the time window down to nano- or pico-seconds with future technical developments. An experimental demonstration of these fast dynamics, we believe, will be an important step in the technique and for a suitably chosen molecule, significant insight may be gained into the very fast photo-chemical and excited state processes at the molecular level.

1. C. E. Singer, B. N. Ames, Sunlight Ultraviolet and Bacterial DNA Base Ratios. *Science* **170**, 822-826 (1970).

2. L. Margulis, J. C. G. Walker, M. Rambler, Reassessment of roles of oxygen and ultraviolet light in Precambrian evolution. *Nature* **264**, 620-624 (1976).

3. E. N. Jacobsen, A. Pfaltz, H. Yamamoto, *Comprehensive Asymmetric Catalysis* (Springer, Berlin, New York, 1999).

4. I. Ojima, *Catalytic Asymmetric Synthesis* (Wiley, Hoboken, NJ, ed. 3, 2010).

5. N. Hoffmann, Photochemical Reactions as Key Steps in Organic Synthesis. *Chem. Rev.* **108**, 1052-1103 (2008).

6. F. Lévesque, P. H. Seeberger, Continuous-Flow Synthesis of the Anti-Malaria Drug Artemisinin. *Angew. Chem. Int. Ed*. **51**, 1706-1709 (2012).

7. R. R. Lunt, N. C. Giebink, A. A. Belak, J. B. Benziger and S. R. Forrest, Exciton diffusion lengths of organic semiconductor thin films measured by spectrally resolved photoluminescence quenching. *J. Appl. Phys.* **105**, 53711 (2009).

8. S. M. Menke, W. A. Luhman and & R. J. Holmes, Tailored exciton diffusion in organic photovoltaic cells for enhanced power conversion efficiency. *Nat. Mater.* **12**, 152–157 (2013).

9. S. Hofmann, T. C. Rosenow, M. C. Gather, B. Lüssem, and K. Leo, Singlet exciton diffusion length in organic light-emitting diodes. *Phys. Rev. B* **85**, 245209 (2012).

10. A. A. High, E. E. Novitskaya, L. V. Butov, M. Hanson and A. C. Gossard, Control of exciton fluxes in an excitonic integrated circuit. *Science* **321**, 229–231 (2008).

11. M.C. Hanna and A. J. Nozik, Solar conversion efficiency of photovoltaic and photoelectrolysis cells with carrier multiplication absorbers. *J. Appl. Phys.* **100**, 074510 (2006).

12. B. Ehrler, M. W. Wilson, A. Rao, R. H. Friend and N. Greenham, Singlet exciton fission-sensitized infrared quantum dot solar cells. *Nano Lett.* **12**, 1053–1057 (2012).

13. D. N. Congreve *et al*. External quantum efficiency above 100% in a singlet-exciton-fission-based organic photovoltaic cell. *Science* **340**, 334–337 (2013).

14. H. Uoyama, K. Goushi, K. Shizu, H. Nomura, C. Adachi, Highly efficient organic light-emitting diodes from delayed fluorescence. *Nature* **492**, 234-238 (2012).

15. Q. Zhang *et al.*, Efficient blue organic light-emitting diodes employing thermally activated delayed fluorescence. *Nature Photonics* **8**, 326-332 (2014).

16. M. A. Green, K. Emery, Y. Hishikawa, W. Warta, E. D. Dunlop, Solar cell efficiency tables (version 46). *Prog. Photovoltaics* **23**, 1-9 (2015).

17. S. Schmidbauer, A. Hohenleutner, B. König, Chemical Degradation in Organic Light-Emitting Devices: Mechanisms and Implications for the Design of New Materials. *Advanced Materials* **25**, 2114-2129 (2013).

18. D. Y. Kondakov, C. T. Brown, T. D. Pawlik, V. V. Jarikov, Chemical reactivity of aromatic hydrocarbons and operational degradation of organic light-emitting diodes. *Jnl. Apl. Phys.* **107**, 024507 (2010).

19. K. Yokoyama *et al.*, Future directions of μSR - laser excitation. *Phys. Scr.* **88**, 068511 (2013).

20. R. Kadono, A. Matsushita, R. M. Macrae, K. Nishiyama, and K. Nagamine, Muonium Centers in Crystalline Si and Ge under Illumination. *Phys. Rev. Lett.* **73** 2724 (1994)

21. K. Ghandi, I. P. Clark, J. S. Lordc and S. P. Cottrell, Laser-muon spin spectroscopy in liquids - A technique to study the excited state chemistry of transients. *Phys. Chem. Chem. Phys.* **9**, 353 (2007).

22. L. Nuccio, L. Schulz, A. J. Drew, Muon spin spectroscopy: magnetism, soft matter and the bridge between the two. *J. Phys. D: Appl. Phys.* **47,** 473001 (2014).

23. D. G. Fleming *et al.*, Kinetic Isotope Effects for the Reactions of Muonic Helium and Muonium with H2. *Science* **331**, 448-450 (2011).

24. S. Baer, D. Fleming, D. Arseneau, M. Senba, A. Gonzalez, Kinetic Isotope Effects in Gas-Phase Muonium Reactions. *ACS Symp. Ser.* **502**, 111-137 (1992).

25. T. Tanaka, T. Takayanagi, Quantum reactive scattering calculations of H + F_2 and Mu + F_2 reactions on a new ab initio potential energy surface. *Chem. Phys. Lett.* **496**, 248-253 (2010).

26. T. A. Claxton, Aspects of muonium chemistry. *Chem. Soc. Rev.* **24**, 437-448 (1995).

27. B. Patterson, Muonium states in semiconductors. *Rev. Mod. Phys.* **60**, 69-159 (1988).

28. S. R. Kreitzman, E. Roduner, Theory of avoided level-crossing relaxation dynamics for axial muonated radicals. *Chem. Phys.* **192**, 189-230 (1995).

29. E. Roduner *The Positive Muon as a Probe in Free Radical Chemistry: Potential and Limitations of the muSR Techniques* (Berlin: Springer-Verlag, 1988).

30. K. Shimomura *et al.*, Pilot experiment for muonium photo ionization in GaAs. *J. Phys: Conf. Ser.* **225**, 012004 (2010).

31. C. J. Rhodes, Muonium - the Second Radioisotope of Hydrogen - and its Contribution to Free-Radical Chemistry. *J. Chem. Soc. Perkin Trans. 2*, 1379–1396 (2002).

32. L. Schulz *et al.*, Importance of intramolecular electron spin relaxation in small molecule semiconductors. *Phys. Rev. B* **84**, 085209 (2011).

33. L. Nuccio *et al.*, Importance of Spin-Orbit Interaction for the Electron Spin Relaxation in Organic Semiconductors. *Phys. Rev. Lett.* **110**, 216602 (2013).

34 Masayoshi Semba, Muon charge exchange and muonium spin exchange in gases. *Hyp. Int.* **65**, 779 (1991).

35. P. Coppo and S. G. Yeates, Shining Light on a Pentacene Derivative: The Role of Photoinduced Cycloadditions. *Adv. Matt.* **17**, 3001-3005 (2005).

36. L Abu-Sen, J. J. Morrison, A. B. Horn, S. G. Yeates, Concentration- and Solvent-Dependent Photochemical Instability of 6,13-Bis(triisopropysilylethynyl)pentacene. *Adv. Optical Mater.* 2, 636–640 (2014).

37. M. J. Frisch *et al.*, *Gaussian09 Revision C.01*, Gaussian, Inc., Wallingford CT, 2010.

38. J. S. Murray, P. Politzer, Statistical analysis of the molecular surface electrostatic potential: an approach to describing noncovalent interactions in condensed phases. *J. Mol. Struct. Theochem* **425**, 107-114 (1998).

39. B. J. Walker, A. J. Musser, D. Beljonne, R. H. Friend, Singlet exciton fission in solution. *Nature Chemistry* **5**, 1019 -1024 (2013).

40. G. M. Akselrod et al., Visualization of exciton transport in ordered and disordered molecular solids. *Nature Communications* **5**, 3646 (2014).

41. R. R. Lunt et al., Exciton diffusion lengths of organic semiconductor thin films measured by spectrally resolved photoluminescence quenching. *J. Appl. Phys.* **105**, 053711 (2009).

Methods

The MuSES project, funded by the European Research Council, recently upgraded the HiFi spectrometer at ISIS to include a tuneable, high-power laser system and associated infrastructure to perform light-pumped, muon-probed measurements. The sample was illuminated with 532 nm light from a 25Hz Nd-YAG laser, with a pulse energy of 91 mJ. The fundamental frequency of ISIS is 50 Hz, so alternate light-on and light-off measurements were gated to different histograms (see Figure 1). The laser system is housed in a light-tight cabin to the side of the HiFi spectrometer, and is routed underneath the floor to the beam entry chambers. The laser beam, after leaving the cabin, was routed toward the instrument by broadband dielectric mirrors (BBDM series from Semrock). The laser was aligned to a target mounted on the cold finger of

closed cycle helium refrigerator (CCR), which indicates the center of the muon beam. The muon beam position was confirmed with a fixed-point CCD camera. The laser pulse was synchronised with the muon pulse using a digital delay generator (Stanford Research Systems, DG645), which triggers the YAG flashlamp and Q-switch with a set time delay. The trigger is defined from the proton extract kicker, either the current pulse or previous pulse, depending on the delay time needed (the crossover between these modes was ~3.5 μs). A liquid cell was designed to allow continuous flow of the solution through the illuminated area, such that the sample is replaced (from a large bath via a peristaltic pump with PTFE tubing) to minimise the effect of any photochemical reactions that may occur. The flow rate was set to approximately 0.1ml/s. The solvent was degassed via a standard freeze-pump-thaw method prior to dissolving the solute, and the entire circulation system was contained in an Argon atmosphere for the duration of the experiment. A 10 mM solution concentration was decided upon by factoring in the muoniated radical formation probability, singlet fission quantum efficiency and light absorption length at the chosen wavelength (532 nm). Further technical details of the new experimental setup are summarised more fully in the SI. Details on the muon technique, and further references, can be found in several articles[22,23,27,28].

The conformational study and subsequent muonium site assignment was performed using Density Functional Theory using the Gaussian 09 package, and taken at the theory level of B3LYP/DGDZVP. This produces a relatively accurate results for the ALC resonant fields for TIPS-Pn (see SI).

Raw experimental data is available on a publically accessible repository (http://data.isis.stfc.ac.uk). Analysed data shown in the figures and DFT calculations will be made available upon request to the corresponding authors.

Acknowledgments AJD would like to acknowledge financial support from the European Research Council (MuSES project, proposal number 307593) and Sichuan University. All authors would like to acknowledge the scientific and technical support provided by the ISIS pulsed muon and neutron source. KW was funded by the Chinese Scholarship Council. PM was funded by Queen Mary University of London, under the Principal's Studentship scheme.

Author contributions KW and PM contributed equally to this work. KW, PM, KY, JSL, FLP, JH, LS, MW, NAM, SZ, PH and AJD performed the experimental work. KY, PM, JSL and AJD designed, built, tested and commissioned the photo-μSR spectrometer (to be described fully elsewhere). PM, KY, JSL, LN, DJD, KS, IW, PH and AJD set-up the experimental equipment for the work reported here. KW, JSL and AJD analyzed and interpreted the musr data. KW and AM performed the DFT calculations. JEA, PH and AJD interpreted the implications of the results. Everyone contributed to writing the paper. AJD conceived the research and managed the project.

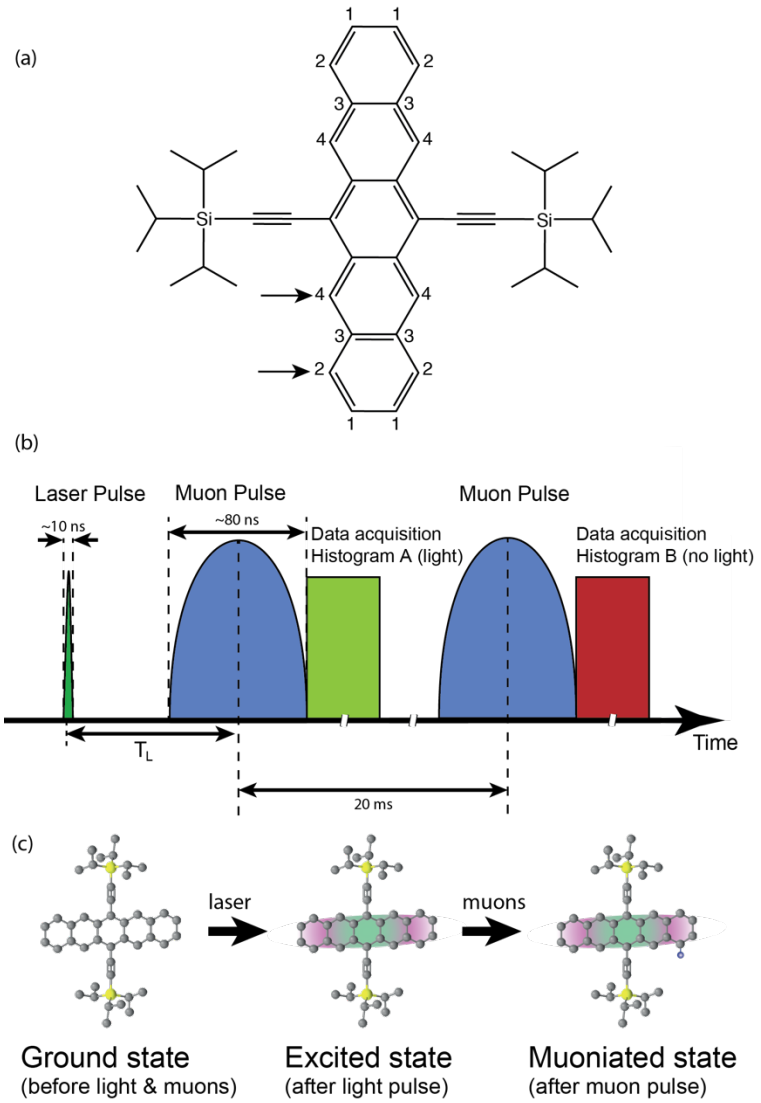

Fig. 1: A schematic illustration of the molecule under investigation and the experimental setup. (a) The molecular structure of TIPS-Pn. The labels are referred to in the text. Sites 1,2 and 4 can support muonium bonding. All similarly numbered sites are equivalent, by symmetry. The arrows correspond to the muonium bonding positions that are probed as a function of delay time, in Figure 2c. (b) The pump-probe pulse structure in our experiments. The laser pulse (dark green) is triggered to arrive prior to the muon pulse (blue), and the delay time between the pulses, T_L, is controllable. The muon pulses are separated by 20 ms, which is determined by the ISIS synchrotron intrinsic frequency of 50 Hz, whereas the laser is fired at 25 Hz. The data is then gated to different histograms, depending on whether a laser pulse directly preceded the muon pulse or not (c) The different stages of the molecule during the experiment. TIPS-Pn starts out in the ground state, without a muon probe present. Upon excitation with light, an excited state is formed as indicated by the green and pink shading, which is subsequently probed with a muonium that bonds to one of the carbons.

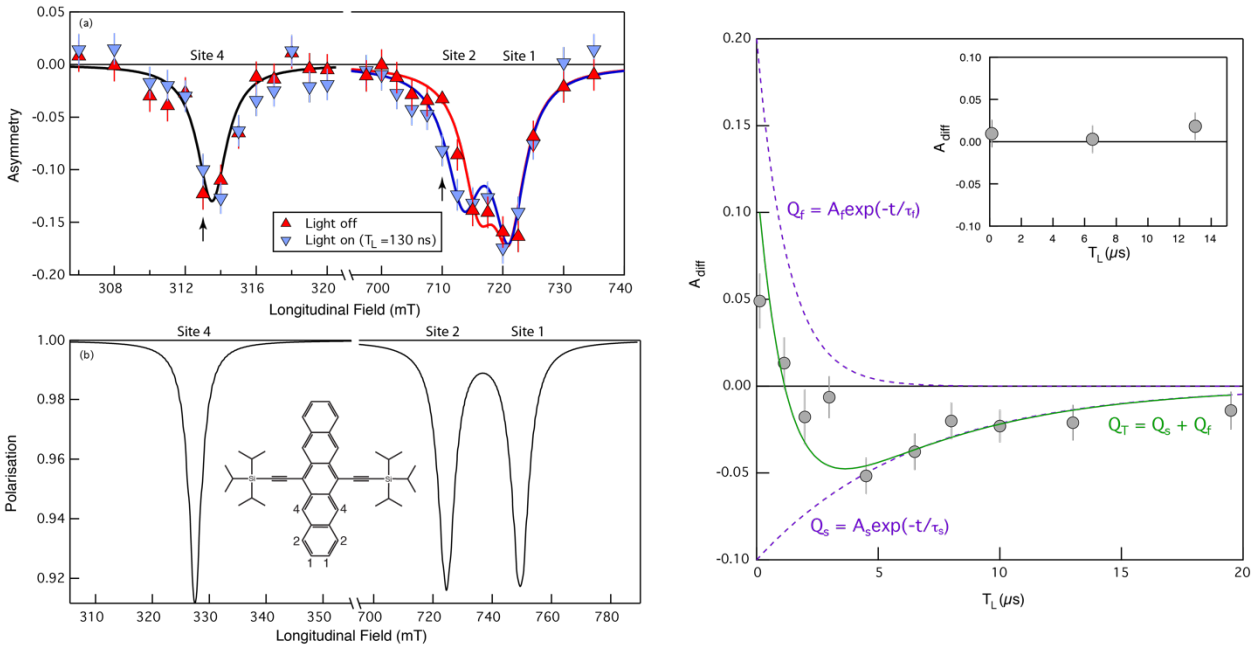

Fig. 2: The time-dependent ALC measurements. (a) ALC spectra with light off (red) and light on (blue) with a pump-probe time delay of 130 ns. There is a clear light-induced change in shape of the two ALCs corresponding to sites 1 and 2, manifesting itself predominantly as a shift in position and an increase in amplitude/area, with the largest changes evident for site 2. The arrows correspond to the fixed fields that were measured as a function of T_L. (b) Predicted lineshapes from DFT calculations (see SI), from which site-assignments can be made. The ALC at around 310 mT corresponds to site 4, whereas there are two ALCs that partially overlap at around 710 mT, corresponding to sites 1 and 2. (c) The pump-probe delay time dependence of the change in amplitude of the ALC at 710 mT, $A_{diff} = A_{off} - A_{on}$. There are two timescales present, one at $\tau_f = 1$ μs and a second at $\tau_s = 6.5$ μs, with opposite signs to the amplitudes A_f and A_s. Lines are guides to the eye, with the lifetimes fixed to values from transient photoabsorption measurements at 1.6 eV and 1.25 eV for τ_f and τ_s, respectively.[35] We note that the statistical error bars as plotted are significantly larger than any systematic errors in this measurement, which is reinforced by the similarity between the two lifetimes derived from the photomusr data, and those extracted from the transient photoabsorption data. Inset: Corresponding data on the ALC at 314 mT, where there appears to be no change in the ALC as a function of time. Where shown, in all panels, errors were calculated by taking the square root of the number of events for each detector group, and propagated using standard error analysis under the assumption of the normal distribution.

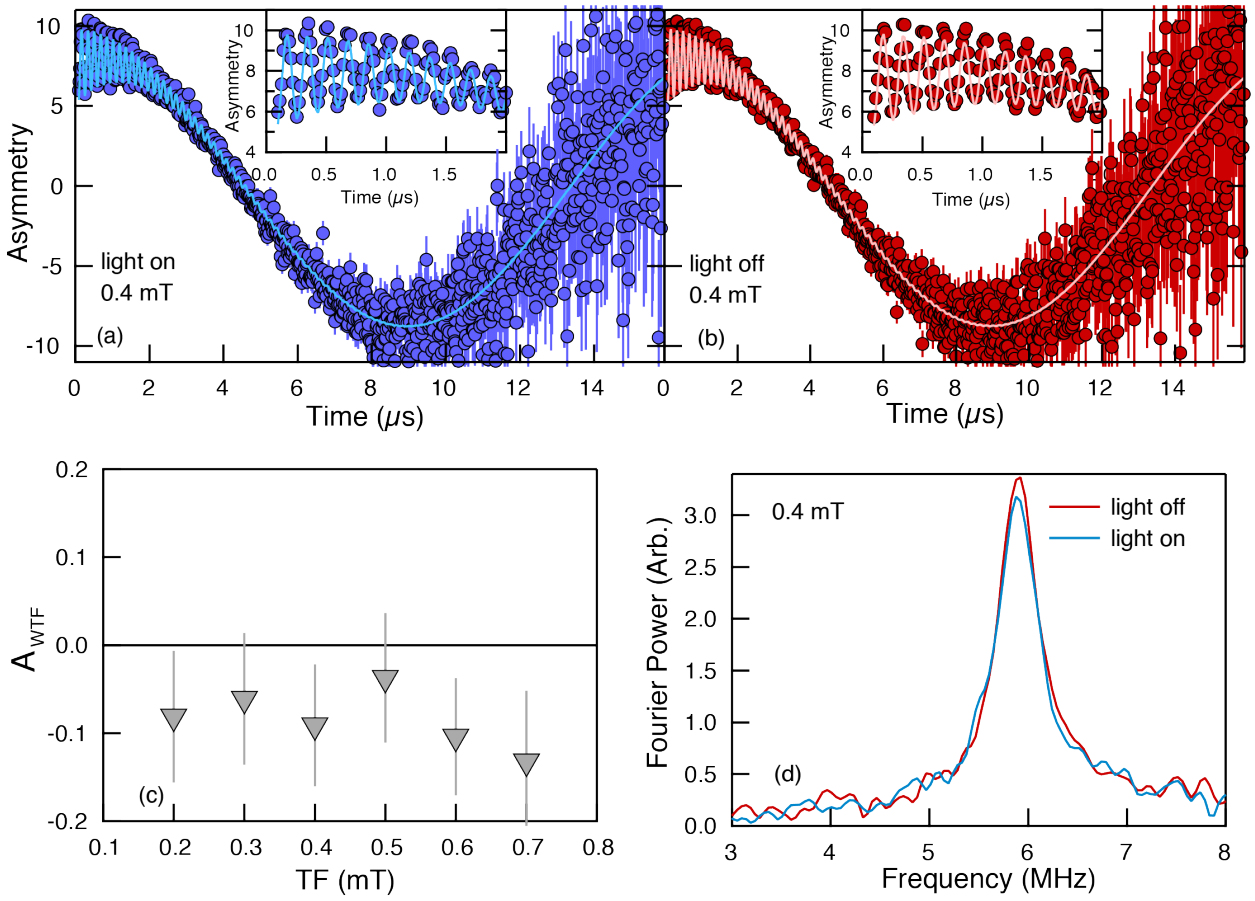

Fig. 3: A variety of muon measurements undertaken to understand the increase in amplitude of the ALC at low times. (a-b) Weak transverse field data for light on (blue) T_L = 130 ns and light off (red), demonstrating that diamagnetic muons (slow precession; main panel) and unbound solvated muonium (fast triplet precession; insets) are present. The data have been fit to a two-component model (see text) to extract light induced amplitude changes to the two components. Errors were calculated by taking the square root of the number of events for each detector group, and propagated using standard error analysis under the assumption of the normal distribution. (c) The light induced change in amplitude of the triplet precession, $A_{WTF} = A_{mu(on)} - A_{mu(off)}$. At all fields measured, there is a net reduction in solvated muonium when excitations are present, and it appears to be field independent. Errors are propagated on the fitted parameters on the assumption of the normal distribution, and represent a 68% confidence interval (standard error). (d) Fourier transforms of the data shown in panels a-b, further demonstrating a light induced change in amplitude, commensurate with a loss of solvated muonium.

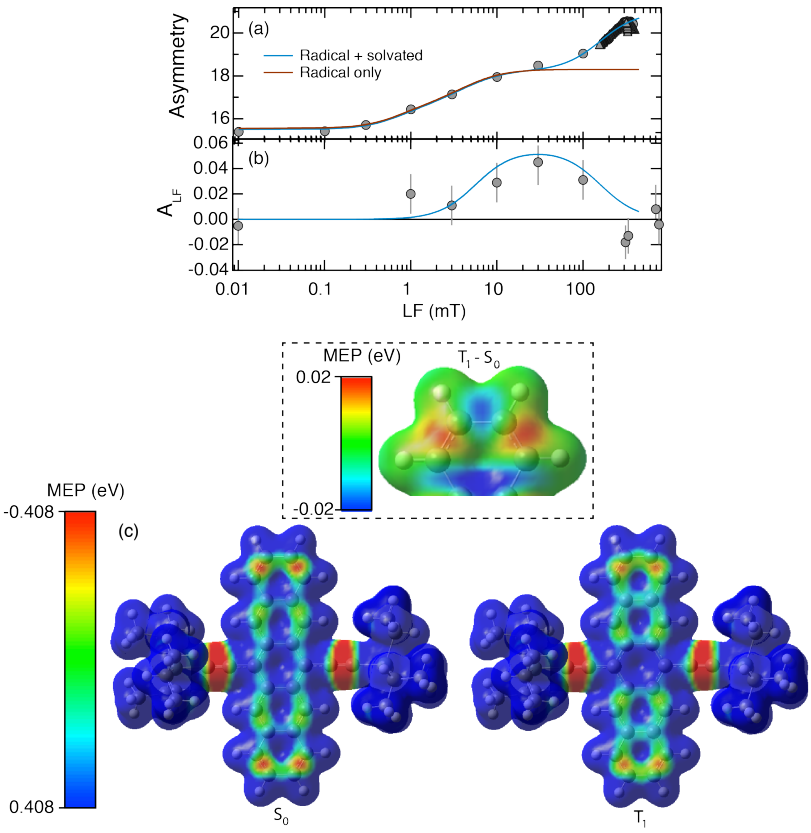

Fig. 4: Consistency checking with ground state muon measurements (a) Longitudinal field repolarization data taken on the EMU spectrometer at ISIS in the ground state, using a well-characterised sample cell made from Ti. The data shows a clear two-step repolarization curve, corresponding to a radical fraction and solvated muonium. The lines correspond to the expected repolarization curve for just a radical (red) and a combined radical and solvated muonium state (blue). HFCs of 80 MHz and 4463 MHz were used for radical and solvated muonium, respectively. Errors were calculated by taking the square root of the number of events for each detector group, and propagated using standard error analysis under the assumption of the normal distribution. (b) The difference between the LF asymmetry for light on and off, $A_{LF} = A_{on} - A_{off}$, for T_L = 130 ns, using the HiFi spectrometer and the laser sample cell. A very small change at intermediate fields is present, which is consistent with a change in reaction rate dynamics in the slow limit or overall population reduction of the solvated muonium (see text). The line is a guide to the eye, representing the functional form expected from light-induced changes. (c) The electrostatic potential map of the ground state S_0 and triplet excited state T_1 generated from DFT calculations (see text). On the end of the backbone, the charge is more spread when the triplet is present, resulting in a reduction in charge around the bond between carbons 1 and 2. This is most easily demonstrated by plotting the difference between T_1 and S_0, which is shown in the top-center of panel (c). Here, the colour-scale is amplified by a factor of 20, such that the red regions demonstrate a reduction in electron density of about 5%, and blue corresponds to an increase in electron density of about 5%.

Supplementary Information:

Density Functional Theory Calculations

In the liquid state, the resonant field of a Δ_0 muon-nuclear spin flip-flop transition, $B^{\Delta 0}$, is determined by both muon and proton isotropic hyperfine coupling constants (HFCCs), A_μ and A_k respectively, and given by[28]:

$$B^{\Delta 0} = \frac{|A_\mu - A_k|}{2(\gamma_\mu - \gamma_k)} - \frac{A_\mu + A_k}{2\gamma_e} \qquad (1)$$

where γ_e , γ_μ and γ_k are the gyromagnetic ratio of electron, muon and proton respectively. Typically, the largest proton HFCC comes from the methylene hydrogen attached to the carbon the Mu bonded to. The Δ_0 resonances due to other nuclei often have negligible intensity due to the small nuclear spin densities[22,28].

Though the calculated isotropic HFCC of the muoniated radical system with DFT is extremely sensitive to multiple factors such as molecular conformation, exchange-correlation functional, basis set and vibrational averaging, so that DFT may not be robust enough in producing the exact HFCCs, the assignment of muonium sites can be successfully addressed due to the systematic feature of the errors.

In terms of the rotational degree of freedom in TIPS-Pn, a variety of different conformers for each muonium site radical are investigated. Since the atoms on the backbone and the two triple bonds are relatively rigid, the initial structures are generated by only twisting the dihedral angles of Si-C-C-H in the three isopropyl groups on each side of TIPS-Pn. Therefore for each muoniated radical there are in total ten different combinations with dihedral angles to be either 0 or 180 degrees. Then the local minima can be found by relaxing the initial conformations, and the isotropic HFCC can be evaluated based on those optimized geometries of all the muoniated radicals.

The isotopic HFCC, $A_{iso,}$ can be calculated by the formul[42]:

$$A_{iso} = \frac{8\pi}{3}\gamma_e\gamma_I \sum_{p,q} < \phi(p) | 2\hat{S}_z \delta(\vec{r}) | \phi(q) > D_{pq} \qquad (2)$$

where γ_e and γ_I are the gyromagnetic ratio of free electron and the nucleus/muon respectively, D_{pq}, is the density matrix, and S_z is the spin operator of electron, $\delta(r)$ is a delta function, indicating that the isotropic HFCC only depends on the spin density at one point, i.e. at the nucleus/muon.

We note that the results of the muonium addition to those possible sites along the triple bonds of the side groups and other sites on the backbone, are not tabulated, because in those radicals there is no corresponding α-proton sharing the spin density distribution, which gives rise to extremely weak proton HFCCs. The consequential ALC resonances are therefore extremely small due to the weak proton HFCCs to which the amplitude of the resonances is directly related[22,25,31]. Table S1 lists the muon and proton HFCC parameters and corresponding ALC resonance fields for many different conformers.

Although for one muon site radical there are many possible structures that can contribute to the ALC resonance, there are a few that are more dominant because they are more likely to exist due to their lower free energies. Figure S1 summarises the relative likelihood of the possible conformers according to their free energies, plotting as a function of the corresponding resonant fields. The relative likelihood is given by the Boltzmann population equation:

$$\eta_{k,\alpha} = \frac{N_{k,\alpha}}{N_{0,\alpha}} = \exp\left(-\frac{E_{k,\alpha} - E_{0,\alpha}}{k_B T}\right)$$

where $N_{k,\alpha}/N_{0,\alpha}$ and $E_{k,\alpha}/E_{0,\alpha}$ is the number and free energy of the kth conformer or the one with the lowest free energy among all the conformers of site-α muoniated radical (α=1,2,4), and the $\eta_{k,\alpha}$ is the relative likelihood of the kth conformer of site-α muoniated radical. The conformational study is taken at the theory level of B3LYP/DGDZVP, which is shown to produce the relatively accurate results for the ALC resonant fields for TIPS-Pn in an investigation into the variation of theoretical HFCCs with the employed functionals and basis-sets[43]. We note here that the method chosen here reduces the computational expense regarding any further vibrational correction, while producing reasonably good estimations for both muon and proton HFCCs.

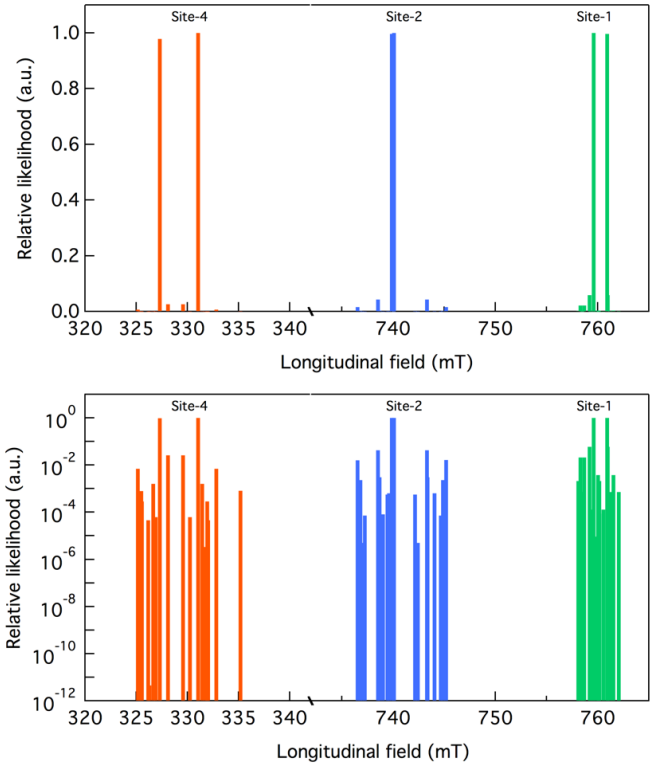

Figure S1: The relative likelihood of the possible structures according to their free energies, plotting as a function of the corresponding resonant fields. All the calculations are performed by package Gaussian09[37] at the theory level of B3LYP/DGDZVP. The y-axis is plotted on a logarithmic and linear scale. A single sharp ALC is observed experimentally for each site.

Initial structures			A_μ(MHz)	A_k(MHz)	$B^{\Delta 0}$ (mT)
Site	Conformation labels				
	Adding direction	Dihedral angles			
4	up	sss-ass	89.2	28.4	325.1
4	up	aaa-aaa	89.2	28.3	325.3
4	down	sss-sss	89.4	28.5	325.5
4	up	sss-aas	89.2	28.3	325.6
4	up	aaa-sss	89.4	28.3	326.2
4	up	aas-ass	89.6	28.2	328.1
4	down	aas-ass	89.8	28.2	329.6
4	down	aaa-aas	89.9	28.1	330.3
4	up	ass-ass	90.1	28.1	331.0
4	up	aas-aas	90.1	28.1	331.4
4	down	aaa-aaa	90.1	28.0	331.7
4	down	sss-aas	90.1	28.0	331.9
4	down	aaa-ass	90.2	28.1	331.9
4	down	aaa-sss	90.2	28.1	332.0
4	down	sss-ass	90.3	28.0	332.8
4	up	sss-sss	90.8	28.1	335.2
2	down	sss-ass	201.5	63.7	736.6
2	down	aaa-ass	201.6	63.7	736.8
2	down	aaa-aaa	201.4	63.5	737.0
2	down	aaa-sss	201.6	63.7	737.2
2	down	aas-ass	201.8	63.6	738.5
2	down	aas-aas	201.8	63.6	738.7
2	down	aaa-aas	201.7	63.4	739.0
2	down	sss-aas	201.9	63.6	739.5
2	up	sss-sss	202.1	63.7	739.6
2	down	ass-ass	201.9	63.4	739.9
2	up	aaa-aas	201.8	63.4	740.1
2	up	ass-ass	201.9	63.4	740.1
2	up	sss-aas	202.3	63.4	742.1
2	up	aaa-aaa	202.2	63.3	742.4
2	up	aas-ass	202.5	63.4	743.3
2	up	aas-aas	202.5	63.4	743.4
2	down	sss-sss	202.7	63.5	744.1

2	up	aaa-sss	202.7	63.3	744.7
2	up	aaa-ass	202.7	63.3	744.9
2	up	sss-ass	202.7	63.3	745.2
1	down	aaa-ass	207.0	65.1	758.1
1	up	sss-ass	207.0	65.1	758.3
1	down	aaa-aaa	207.0	65.1	758.5
1	up	sss-aas	207.2	65.3	758.5
1	down	sss-ass	207.0	65.0	758.7
1	down	aas-ass	207.3	65.2	759.2
1	down	aaa-aas	207.2	65.2	759.3
1	down	aaa-sss	207.3	65.1	759.6
1	down	ass-ass	207.3	65.2	759.6
1	up	aaa-aaa	207.2	65.0	759.9
1	down	aas-aas	207.5	65.2	760.0
1	up	sss-sss	207.5	65.2	760.1
1	up	aaa-ass	207.3	65.0	760.2
1	up	aaa-sss	207.4	65.1	760.2
1	up	aaa-aas	207.4	65.1	760.6
1	up	ass-ass	207.5	65.1	760.9
1	up	aas-ass	207.5	65.1	761.0
1	down	sss-sss	207.6	65.2	761.2
1	up	aas-aas	207.7	65.2	761.5
1	down	sss-aas	207.7	65.1	762.1

Site	A_μ(MHz)		A_k(MHz)		$B^{\Delta 0}$ (mT)	
	Min.	Max.	Min.	Max.	Min.	Max.
1	207.0	207.7	65.0	65.2	758.1	762.1
2	201.4	202.7	63.3	63.7	736.6	745.2
4	89.2	90.8	28.0	28.5	325.1	335.2

Table S1: The results of muon and proton HFCC (A_μ and A_k) and the corresponding ALC resonance field ($B^{\Delta 0}$) of muoniated TIPS-Pn with Mu adding to site 1, 2 and 4, relaxing from different initial structures. The 'adding directions' indicate adding towards either the 'up' or 'down' side of the backbone plane of TIPS-Pn. The dihedral angle of Si-C-C-H in the isopropyl groups on two sides of TIPS-Pn is set to be either 0 or 180 degree, labelled as 's' or 'a' respectively. Therefore the conformational changes due to the dihedral angles are labelled as 'aas-ass' etc., which indicates there are two 180 degree angles and one 0 degree angle on one side, with two 0 degree and one 180 degree angle one the other side. All the calculations are performed by package Gaussian09[37] at the theory level of B3LYP/DGDZVP. The lower panel shows the ranges of calculated parameters, summarising the data in the upper panel.

The site-4 radical can be assigned unambiguously as its Δ_0 resonance fields are far away from those from the other muon sited radicals, as can be clearly seen from the Table S1 and Figure S1. The Figure S1 also shows that all the ALC resonant fields from the site-2 muoniated radical are lower than that of the site-1 radical, even though they have the HFCCs very close to each other. We tentatively assign the three visible ALC resonances, at ~313 mT, ~715 mT and ~720 mT, in our experiment to be site-4, site-2 and site-1 respectively.

However, there is still some ambiguity in the assignment of site-1 and site-2 because in the ALC spectra nearly overlap each other. Since the actual values of HFCCs are also extremely sensitive to the level of theory, i.e. the combination of exchange-correlation functional and basis-set, one would be more convinced by the comparison between the results of site-1 and site-2 at different theoretical levels. In addition to the *B3LYP/DGDZVP*, we had a study with two more exchange-correlation functionals, CAM-*B3LYP* wB97XD, and two more basis-sets, *DGDZVP2* and cc-pVDZ. Table S2 shows the results.

	B3LYP/ cc-pVDZ			CAM-B3LYP/cc-pVDZ			wB97XD/cc-pVDZ		
Site	Aμ (MHz)	Ak (MHz)	B (mT)	Aμ (MHz)	Ak (MHz)	B (mT)	Aμ (MHz)	Ak (MHz)	B (mT)
1	183.3	57.5	672.41	222.1	69.7	814.37	210.9	66.1	773.89
2	176.1	55.0	647.02	208.4	65.5	763.75	195.6	61.5	716.82
	B3LYP/DGDZVP			CAM-B3LYP/DGDZVP			wB97XD/DGDZVP		
1	205.3	64.5	752.78	250.1	78.5	917.21	236.3	74.2	866.35
2	198.5	62.3	727.81	237.6	74.7	870.55	219.1	71.2	790.13
	B3LYP/DGDZVP2			CAM-B3LYP/DGDZVP2			wB97XD/DGDZVP2		
1	204.5	64.2	749.95	247.9	77.8	909.40	235.0	73.7	861.99
2	198.9	62.6	728.52	236.9	74.4	868.32	223.5	69.7	821.88

Table S2: The comparison between the results of site-1 and site-2 at different theoretical levels. In addition to the B3LYP/DGDZVP *used in Table S1, we used two more exchange-correlation functionals,* CAM-B3LYP *and wB97XD, and two more basis-sets,* DGDZVP2 *and cc-pCDZ. All the calculations are performed by package Gaussian09*[37].

As can be seen from the Table S2, the overestimation or underestimation on HFCCs comes out in the same measure for both the site 1 and 2 radicals, and the ALC resonant fields of site-2 at all the different theory levels are lower than those of site-1, no matter how the absolute values varying with the functional and basis-set. Therefore, we can conclude that the three ALC resonances shown in Figure 2 from low to high fields are indeed site-4, site-2, and site-1 radicals respectively.

Photo-μSR experiments

The MuSES project, funded by the European Research Council, recently upgraded the HiFi spectrometer at ISIS to include a tuneable, high-power laser system and associated infrastructure to perform light-pumped, muon-probed measurements. The technical details of the new experimental setup are summarised here, but further technical details of the new spectrometer are in preparation for submission elsewhere. Details on the muon technique, and further references, can be found in several articles[22,23,27,28].

Laser system was manufactured by Litron Ltd and has a tuneable wavelength (200–2400 nm) provided by a high-power Nd–YAG backing an Optical Parametric Oscillator (OPO). The Nd–YAG operates at 25Hz, whilst the fundamental frequency of ISIS is 50 Hz, allowing alternate light-on and light-off measurements to be gated to different histograms (see Figure 1). The fundamental and four harmonics (1064, 532, 355, 266 and 213 nm) are available directly from the Nd-YAG for use in the case these fixed wavelengths are suitable and photon count is important. For example, the current system has 2.1 J per ~16 ns pulse available at 1064 nm, whereas up to 23 mJ per pulse is available from the wavelength tuneable OPO, depending on the wavelength. The laser system is housed in a light-tight cabin to the side of the HiFi spectrometer, and is routed underneath the floor to the beam entry chambers (BEC), either on the side or the back of the HiFi spectrometer, as shown in Figure S2a. The entry port on the side of the spectrometer allows the front of the sample to be illuminated, either by holding it at 45 degrees to the muon beam or by a complex set of optics. The rear port allows the sample to be illuminated from the back, and was the chosen geometry for the experiments reported here.

The laser beam, after leaving the cabin, is routed toward the instrument by broadband dielectric mirrors (BBDM series from Semrock) contained in the red mirror boxes shown in Fig. S2a. Each mirror box has an optical breadboard in the bottom to set up mirrors. The beam is aligned using a 405 nm Class II diode laser (DL) situated on the optical table in the cabin. At the sample position, the DL beam is aligned to a target mounted on the cold finger of closed cycle helium refrigerator (CCR), which indicates the center of the muon beam. The muon beam position was confirmed with a fixed-point CCD camera. Once the beam path is defined, the laser beam used in our experiments follows it. Fig. S2b shows the optical setup in the beam entry chamber (BEC). The beam coming out of the periscope is reflected and levelled to the correct height, and directed to the spectrometer. The partial reflection aligned to a target is monitored by a camera to track the position over the course of the experiment. Laser power was measured in front of the exit port of BEC using a power sensor. The measured pulse energy is calibrated with another power sensor in the laser cabin, which measures a partial reflection from a beam sampler, therefore the pulse energy on sample is live-monitored and recorded over the course of the experiment.

The laser pulse was synchronised with the muon pulse using a digital delay generator (Stanford Research Systems, DG645), which triggers the YAG flashlamp and Q-switch (QSW) with a set time delay. The trigger is defined from the proton extract kicker, either the current pulse or previous pulse, depending on the delay time needed (the crossover between these modes was ~3.5 μs). The delay generator sends a signal to the muon data acquisition equipment (DAE) to sort the data bins for the “Light ON” and “Light OFF” spectra. The “time zero” – when the center of the muon pulse corresponds to the center of the laser pulse at the sample position – is measured directly using a scintillator and photomultiplier tube. The muons create light as they

pass through and stop in the scintillator, whereas we measured the light from the laser directly. Both sources of light are subsequently measured by the photomultiplier tube.

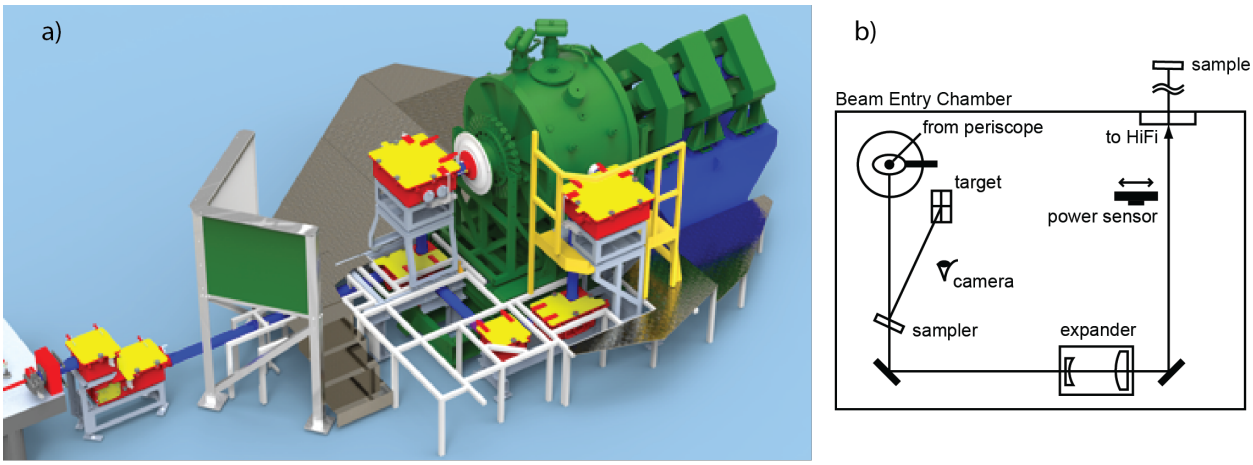

Figure S2(a): The upgraded HiFi spectrometer. The beam tube (blue) exits the laser cabin (not shown) and is routed underneath the floor via mirror boxes (red and yellow) into the HiFi spectrometer (green) either from the side or the back.(b) A schematic diagram of the beam entry chamber.

A liquid cell was designed to allow continuous flow of the solution through the illuminated area, such that the sample is replaced (from a large bath via a peristaltic pump with PTFE tubing) to minimise the effect of any photochemical reactions that may occur. The flow rate was set to approximately 0.1ml/s, such that the illuminated region of the cell was entirely replaced roughly every half a second. The solvent was degassed via a standard freeze-pump-thaw method prior to dissolving the solute, and the entire circulation system was contained in an Argon atmosphere for the duration of the experiment. The sample cell is shown in Figure S3. Monte Carlo simulations of the sample cell were performed using the GEANT package[44] to estimate the optimum muon/laser window separation, and which was subsequently adjusted via tightening the screws that press the windows into indium seals. A 10 mM solution concentration was decided upon by factoring in the muoniated radical formation probability, singlet fission quantum efficiency and light absorption length at the chosen wavelength (532 nm). Further details of this procedure, as well as the technical details of the spectrometer, has been and will be published elsewhere[19,45,46].

Importantly, the gating of light-on and light-off data into different histograms on a per-pulse basis self-corrects for any long-term beam stability, drift or other systematic issues with the accelerator or experimental equipment. The measurement sequence is depicted in Figure 1b. This enables one to directly compare *amplitudes* of ALC spectra, which can be notoriously difficult to do, due to the uncertainties of geometrical differences and systematic errors associated with the experiments.

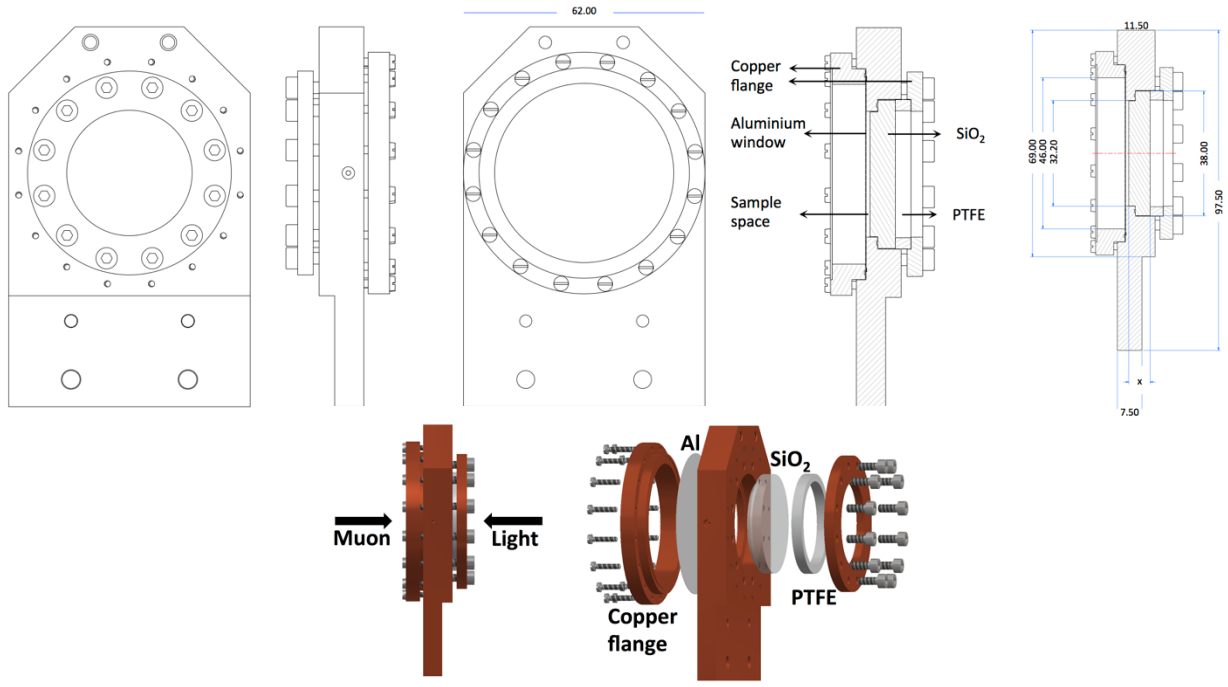

Figure S3: The sample cell. Dimensions shown are in mm.

Estimation of the fraction of excited molecules in the cell

Energy of the laser pulse	= 91 mJ
Energy of a photon at 532nm	= 3.73×10^{-16} mJ
Number of photons per pulse	= 2.44×10^{17}
Area of the laser spot	= 177 mm^2
Thickness of the cell	= 0.45 mm
Number of molecules in the cell at a 10mM concentration	= 4.79×10^{17}
Ratio of molecules excited to number of molecules	= 51%

At the concentrations used, the triplet efficiency is about 100% - i.e there will be approximately 4.8×10^{17} triplet excitations generated. However, we note that this estimation does not take into account the stopping profile of the muons or the exponential penetration depth of the light, as well as solvated muonium diffusion. These detailed and technically challenging calculations will be published in due course[45]. We note that with a flow rate of approximately 0.1 ml / second, each molecule will have been excited around 10 times before it is replenished.

Temperature Dependent ALCs

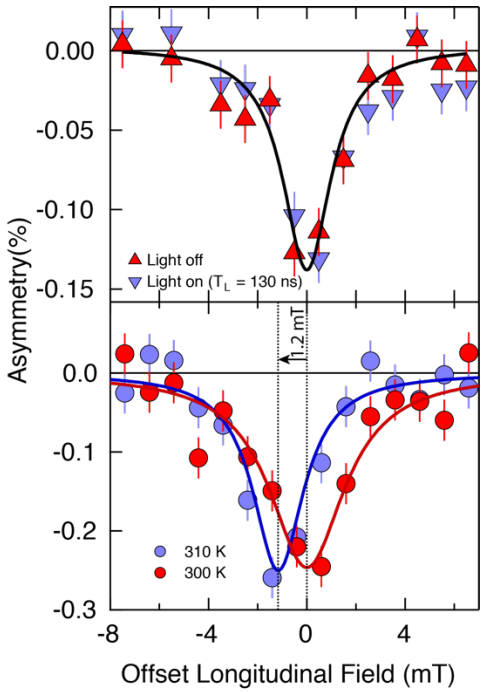

Figure S4: Top – ALC for site 4 from Figure 2 in the main paper, replotted with the field normalised to the peak position so that a direct comparison can be made with the lower panel. It is evident that there is no shift in the ALC position when light is present, in contrast to the ALCs for sites 1 and 2. Bottom – the same ALC (also site 4), but taken on the EMU spectrometer using a standard Ti liquid cell for two different temperatures. A very clear reduction of ~1.2 mT in the ALC position is evident with a 10K increase in temperature. This is absent in the top panel, which shows light induce changes. This is consistent with our conclusion that the laser induced effects observed for sites 1 and 2 are not related to a temperature increase, as there would be a temperature dependent shift in the site 3 ALC position.

Fourier Transforms of Low TF Data

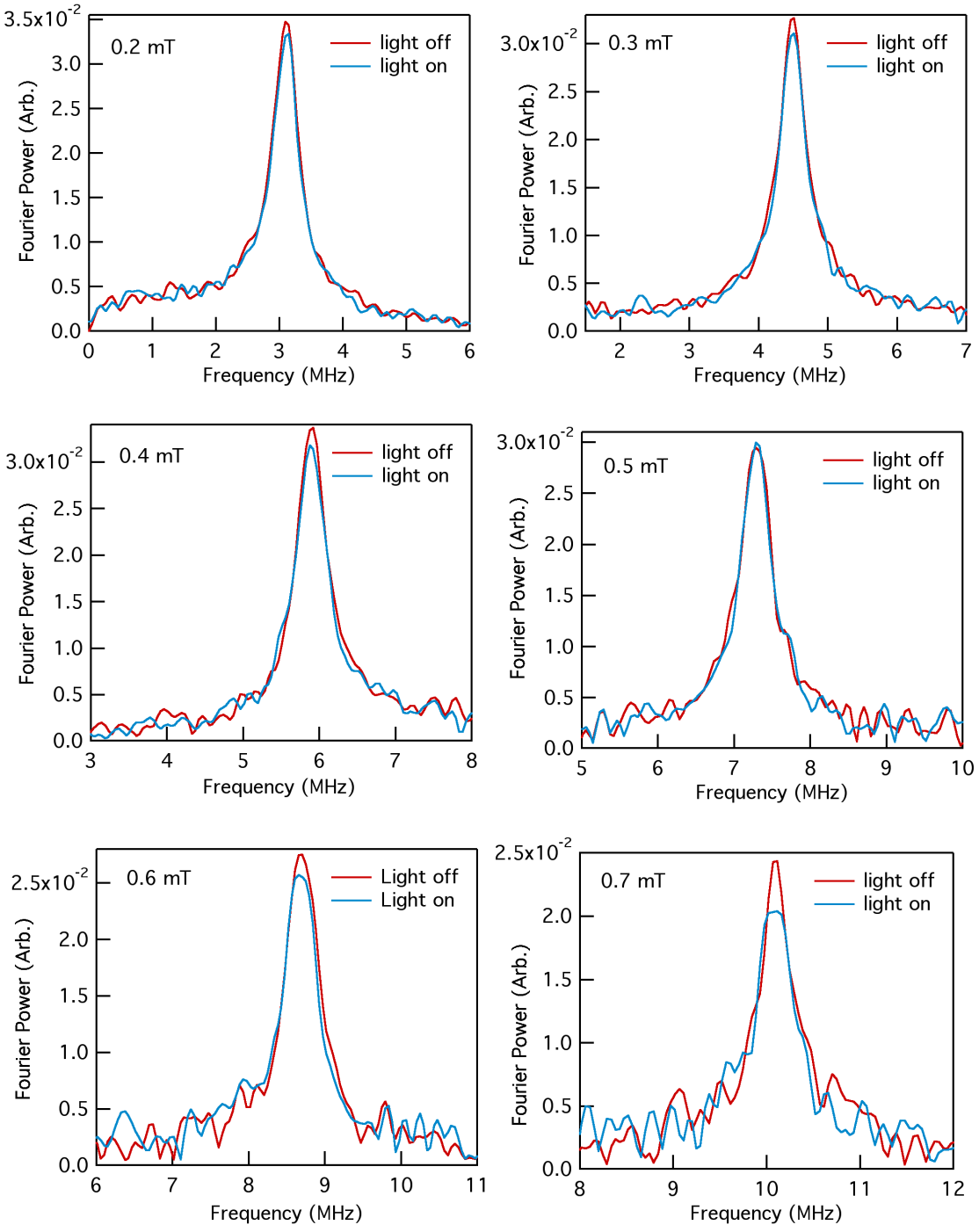

Figure S5: The Fourier transforms of the low-TF data for light-on and light-off for T_D = 130ns. The amplitude of this represents the amplitude of triplet precession of solvated muonium. It is clear that for all fields, except 0.5 mT, there is a clear reduction in signal amplitude and slight increase in width, when the light is on. This indicates the solvated muonium component is smaller when the light pulse is present.

Quantitative analysis of the ALC

There is a clear change in position in the two Δ_0 ALC spectra centered on ~ 715 mT in Figure 2a of the manuscript. The area underneath an ALC is related to two main phenomena – the underlying formation probability and the value of the HFCCs (proton-electron and muon-electron). If the small shift in the lineshape represents a change in HFCC, whether it can account for the change in amplitude/area should be addressed. It is difficult to quantitatively assess the change in shape, amplitude and position via fitting a double Lorentzian, as there are an insufficient number of data points for the two overlapping lineshapes. The area underneath the curves, however, can be easily estimated via a simple numerical integration. The area underneath the ALCs at ~715 mT is 0.907 ± 0.004 with light off, compared to 0.971 ± 0.004 with light on, representing a roughly 7% increase in area when light is present. We note that the baseline is determined by a finite number of points, with error bars of their own, which will contribute to the error on the integrated area of the line. However, the baseline is the same for light on and off so it does not contribute to the error on the difference.

We have estimated the largest shift in ALC position, B_r, as -3 mT. A -3 mT shift of B_r can either be explained in terms of an increase in A_k or a reduction in A_μ. Shown in Figure S6 is the dependence of Br on A_k and A_μ, from which it is clear that there would need to be approximately a 0.5 MHz change in either A_k and A_μ to account for a ~3 mT shift in B_r. Using the Quantum programme[47], we have calculated the ALCs for three conditions: A_μ = 200 MHz and A_k = 70 MHz which are sufficiently representative values of the HFCCs for site 2, two further ones with a 0.5 MHz increase/reduction to A_k and A_μ, respectively. This is shown in Figure S7, where it is clear that the area change is marginal. The change in area due to a reduction in A_μ is 0.003%, whereas the change in area due to an increase in A_k is 0.024%, compared to a 7% increase in area in the experimental data.

In principle, it may be possible for the changes in ALC position due to A_k and A_μ to almost cancel each other out (the ALC position increases as A_μ is increased, but decreases as A_k is increased; see Figure S6). The increased proton coupling constant would then dominate the increased area underneath the ALC. The change to both of them would need to be relatively large but very similar, with a relative difference of ~0.5 MHz to account for the change in position of the ALC – for example, around 49.5 MHz increase in A_μ and a 50 MHz increase in A_k. This fortuitous cancellation is extremely unlikely. Nonetheless, an example of this is shown in the left panel of Figure S8 for a comparison of A_k = 70 and A_μ = 200 with A_k = 120 MHz and A_μ = 250 MHz. There is a significant increase in width for the modified HFCCs, with a minor change in position. However, also shown in Figure S8 (middle panel) is the LF repolarisation curve that one would expect from such a large increase in both A_k and A_μ. The difference is shown in the right hand side panel of Figure S8, using the same definition as used in the main manuscript (Figure 4b). Note that it has an opposite sign to the observed light induced change in the data (see Figure 4b for comparison). The only way one would be able to have the same sign as is observed in the data, is to have a *reduction* in A_k and A_μ; however, this would result in a less broad ALC with a lower area. We note that a reduction in the quantity of solvated muonium and a commensurate increase in the quantity of bonded muonium would result in a change to the LF repolarization curve of the correct sign, as is evident in Figure 4b of the main manuscript.

It is therefore not possible to account for the increase in ALC width/amplitude solely in terms of light induced changes to the hyperfine coupling constants, despite the likelihood of such changes being present. Given the commensurate reduction in unbound triplet muonium precession

(Figures 3 and S5), and the light-induced changes to the LF repolarization curve, it is our conclusion that light induced changes in the reaction rate of unbound muonium with the molecule are responsible for the main changes observed in the ALCs in Figure 2.

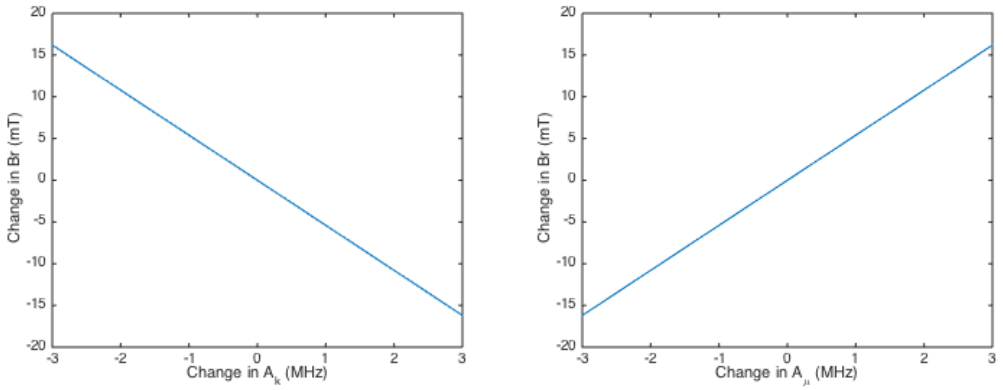

Figure S6: The change in B_r as a function of A_k and A_μ.

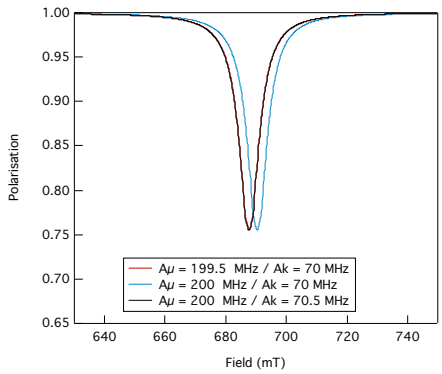

Figure S7: Comparison of ALC spectra for a 0.5 MHz shift to A_k and a -0.5 MHz shift to A_μ, which will both result in a ~3 mT reduction in the position of the ALC. The largest change in area is 0.02% (see text), compared to more than 7% in the data.

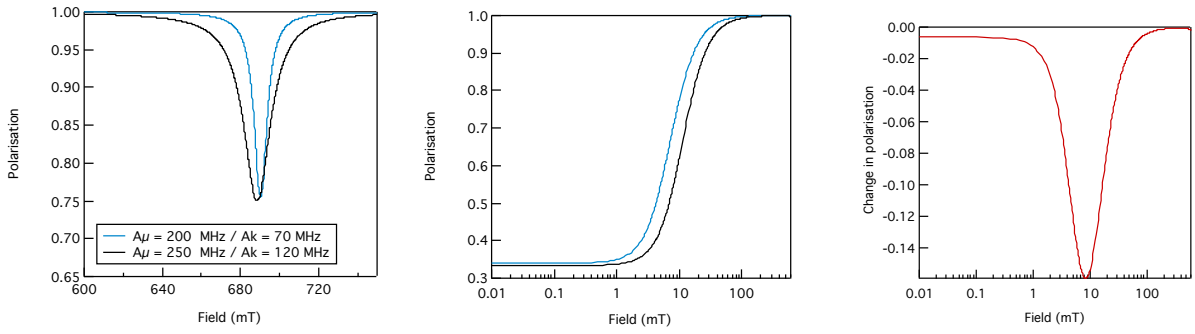

Figure S8: Left: Comparison of ALC spectra for a 50 MHz change to both A_k and A_μ. This will result in an apparent increase to the width/area of the Lorentzians that are fitted to the ALC spectra, without a significant change to the position. Middle: there is a commensurate change in the LF repolarization curve. Right: The difference between the two repolarization curves shown in the middle panel. Note it is negative; the difference between light on and off data has the opposite sign using the same definition of "difference".

A note on errors

Throughout this manuscript, all errors are calculated on the explicit assumption that Poissonian statistics apply. Specifically, when assuming Poissonian statistics, the statistical error on the number of counts on a given detector is given by the square root of those number of counts. Errors on derived quantities – such as experimental asymmetry – are then calculated via standard error propagation. However, this treatment is clearly only correct for random errors, and we have not explicitly quoted systematic errors, as they are either identical for the light on/off difference or they are small.

Sources of systematic errors in a photomusr experiment are quite varied. The major examples are:

1. Drift in the position of the laser spot. The most likely cause of this is very small changes in the angle of the mirrors as a function of time, which is amplified at the sample position as a result of the long throw distance between the laser and sample. Large changes in beam spot position can be observed, since the laser spot is continuously monitored via a camera, but relatively small changes (of a one or two mm) may not be easily seen. The result would be a change in the amplitude in the light induced signal. However, this drift happens over a significant length of time – many hours, if not days. Since the laser is running at 25 Hz whilst the muons are at 50 Hz, and each drift within a run is entirely averaged out in the ~1e5 pulses in each light on/off histogram. All ALC curves are scanned at least twice to ensure that drift is not significantly affecting the light induced signal at different magnetic fields. The time delay measurements were measured in a random order, to ensure that drift does not play a role in the excitation timescale measurements.
2. Drift in the laser power. There are several causes of laser power drift. It could be due to long-term damage to the optics, or more likely, a temperature variation of the laser. This drift also has a long timescale – hours or days – and is similarly mitigated by the same measures as in point 1.
3. Drift in the muon beam spot position. There are many factors that can change the size or position of the muon spot, with one of the more likely to be as a result of drift in the power supplies of the electromagets responsible for directing and focussing the muon and/or proton beams. It would typically manifest itself as a change in asymmetry of both light on and light off data, which should be the same in both given the 25 Hz laser and 50 Hz muon beam. It should therefore not affect the light induced changes observed, but if the timescale of this drift is longer than the separation of each measurement on a particular scan, it can modify the background. This is usually fitted so that the off-resonant data is flat. If single points on a scan are away from the general trend (outliers) in the data, then they are re-measured. A particularly robust way of identifying the outliers is to plot the up-down and left-right asymmetry (by grouping the detectors differently in the analysis). An example is shown in Figure S9b, where in addition to a very clear step-change is observed when changing the applied field from ~300 mT to ~700 mT, there there are two outliers on the trend. Long-term drift is also evident in the data.
4. Changes to deadtime as a result of a reduced counting rate. This is usually as a result of an unstable muon beam, and even though it will not affect the light-induced signal, we

paused measurements until the beam became stable again, as background subtraction tends to be difficult in these circumstances. If a small number of points were affected, they were measured a second time. Otherwise the entire scan was repeated.

One final source of systematic errors is incorrect background subtraction. The field dependent background on the HiFi instrument is somewhat complex over the full field range available. It is mainly related to the trajectory of moving charged particles in a magnetic field (muons and positrons) and the subsequent absorption in material surrounding the sample, such as the sample holder. It is typically cyclical, with a period of around 1T, but is strongly dependent on the geometry of the experiment (e.g the shape and amount of material in the sample holder). Fortunately, this geometry does not change when the light is present, and so in our experiments the same background is used for both light-on and light-off data. Importantly, over the restricted field range of the ALCs in our experiments, the background varies very slowly, and a linear or a polynomial function is a good approximation. An example is shown in Fig S9. It is very clear that background is not important in our measurements. The precise choice of function or parameters will not change the results, especially for the light on/off difference. In the figure below, only the light off data was considered for the background substraction (unlike in the main paper); background subtraction would be just as effective if light on, or an average of the two were used.

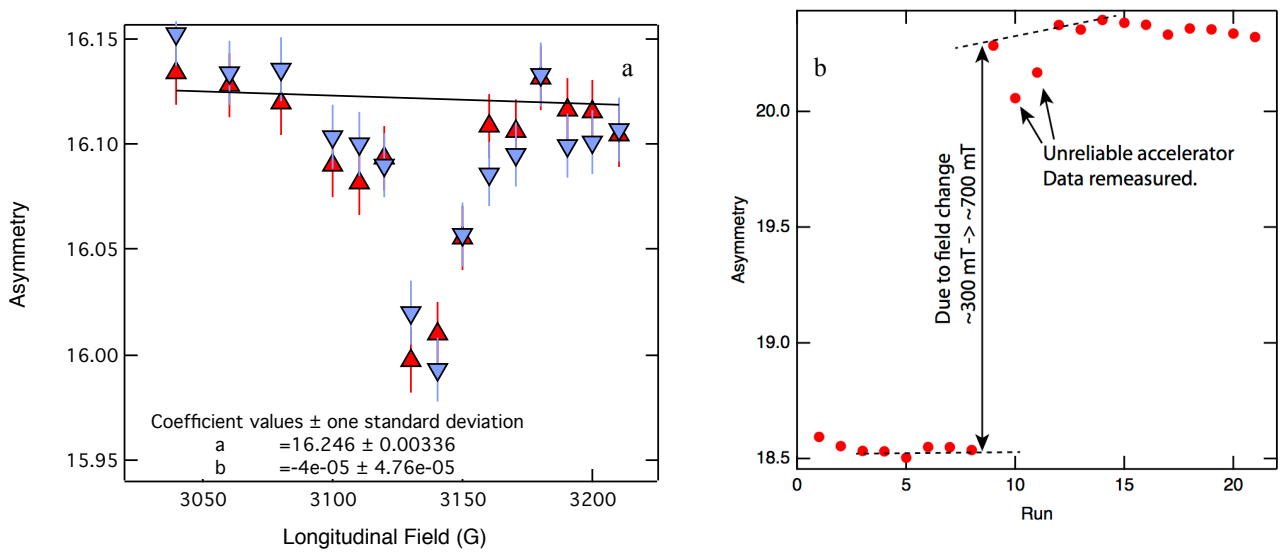

Figure S9 a: An example of one of the many ways to background subtract data. b: An example up-down asymmetry, where two outliers are present, as a result of a change in the muon beam spot position.

Origin of the fast precession in low transverse field

It is likely that Mu also adds to the "alkyne" triple bond in the side-group, forming two states that may be described as phenylacetylene (for those muonium bonding to the carbon close to the backbone) or trimethylsilylacetylene (for those muonium bonding to the carbon close to the Si), possibly with a relatively high rate constant.[48,49] The corresponding resonances would be found outside the field range displayed in Fig. 2 of the manuscript, although it is likely that they will have a relatively low asymmetry due to a small proton-electron HFC constant. In the limit of low proton-electron HFC constant, the fast triplet precession observed in Figure 3 of the main manuscript may be due to precession of the Mu bonded to the triple bond, and any light induced change in this would be indistinguishable from a light induced change of the solvated Mu. Here, we demonstrate that the fast triplet precession cannot be explained by the radical with the Mu bonded to the triple bond and no α-proton. Table S5 shows the proton isotropic HFC constant for the phenylacetylene adduct for *every* proton on the molecule and the muon isotropic HFC constant, calculated with Gaussian09 at the theory level of B3LYP/DGDZVP, with an associated site labelling diagram in Figure S9.

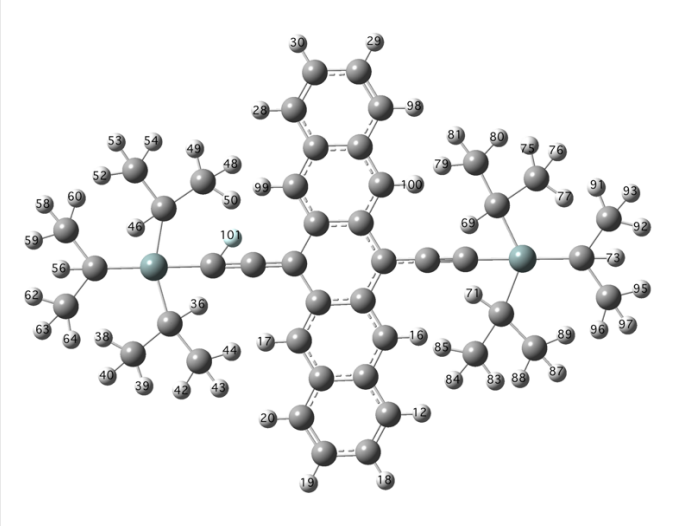

Figure S10: The TIPS-Pn molecule with the H atoms included to enable site assignment for Table S5. Atom 101 is the muon.

It is immediately clear that whilst the proton HFC constant is significantly smaller than muonium that is bound to the back-bone, they are not negligible. For the case of trimethylsilylacetylene adduct, similar proton HFC constants are found but the muon HFC constant is calculated to be approximately 400 MHz. No experimental evidence has been found for this adduct in the solid state, so we only focus on the phenylacetylene adduct. Moreover, the proton HFC constants are similar for both adducts and the relative insensitivity of the triplet precession to the muon HFC constant. To assess whether the muonium bound to the alkyne group, we have performed calculations using the Quantum programme for A_μ = 92.5 MHz and A_k = 0, 1 and 5 MHz. in a 0.4 mT transverse field. The time spectra are shown in Figure S11a. It is very clear that a proton HFC constant of 1 MHz has a significant affect on the polarization. Thirteen such protons exist with a HFC constant greater than 1 MHz. Given the spectra in Fig S11b, it is quite likely that when several proton HFC constants are included, they will destructively interfere resulting in a rapid polarization loss. Upon performing a calculation with eight different proton HFC constants from Table S5, this is clearly demonstrated; there is a rapid polarization loss by around 50 ns,

which is faster than can be measured at the ISIS muon source. If one were to include all of the proton HFC constants in Table S5, this could only be worse; we are unable to do so due to limitations on computational time. We therefore conclude that any muonium reacting on the triple bonds does not contribute to the fast triplet precession shown in Figure 3 of the main manuscript.

Atom Number	A_k(MHz)		Atom Number	A_k(MHz)
H 12	-4.9381		H 62	0.24943
H 16	-14.235		H 63	-0.0078
H 17	4.78555		H 64	-0.01171
H 18	2.9157		H 69	-0.21781
H 19	-5.93367		H 71	-0.21314
H 20	3.17547		H 73	-0.30086
H 28	3.17873		H 75	0.22899
H 29	2.9193		H 76	-0.00337
H 30	-5.93965		H 77	0.28972
H 36	0.2465		H 79	-0.00647
H 38	-0.00702		H 80	0.21017
H 39	0.10359		H 81	0.31022
H 40	0.12379		H 83	0.86232
H 42	0.094		H 84	-0.05685
H 43	-0.00357		H 85	0.13044
H 44	0.11635		H 87	0.11491
H 46	0.00103		H 88	0.14269
H 48	-0.00698		H 89	-0.01389
H 49	0.08915		H 91	-0.03289
H 50	0.0591		H 92	0.0837
H 52	-0.01152		H 93	0.14188
H 53	-0.00859		H 95	1.00185
H 54	0.23599		H 96	0.13988
H 56	-0.01116		H 97	-0.06772
H 58	0.06063		H 98	-4.94484
H 59	0.09441		H 99	4.79078
H 60	-0.00461		H 100	-14.25704
Atom	A_μ(MHz)			
Mu	92.5			

Table S5: The results of muon (A_μ) and proton HFCC (A_k) for all hydrogens in the molecule for the phenylacetylene adduct, using Gaussian09[37] at the theory level of B3LYP/DGDZVP. A site labelling diagram is shown in Figure S10. There are a thirteen proton HFCCs that have a value in excess of ±1 MHz, with two being approximately -14 MHz. The calculated value of A_μ is similar to the experimental value in the solid state (Δ_1 ALC resonance in a polycrystalline sample).[32]

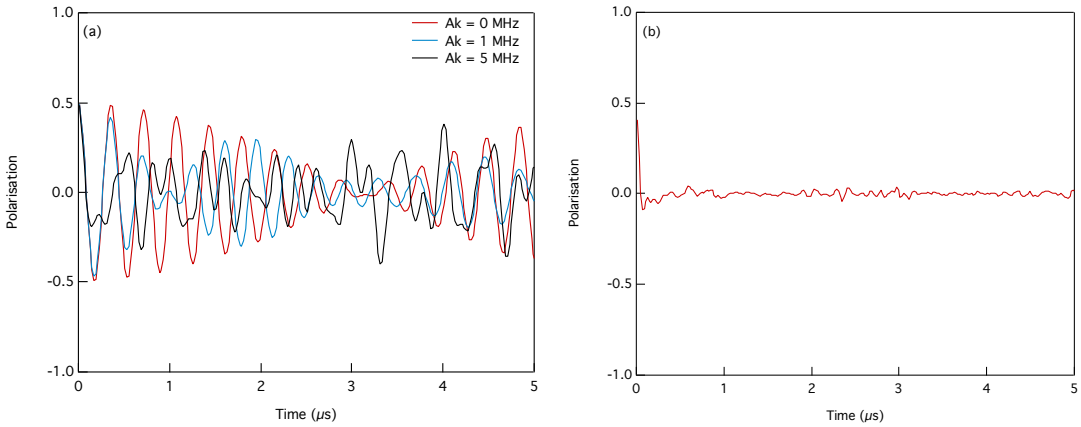

Figure S11: (a) The muon's spin polarization as a function of time, calculated for A_μ = 92.5 MHz and A_k = 0, 1 and 5 MHz, at a transverse field of 0.4 mT. It is clear that a proton HFCC of just 1 MHz has a significant affect on the precession. (b) A calculation for an ensemble of 8 proton HFCCs. Representative values chosen are -4.9381, -14.235, 4.78555, 2.9157, -5.93367, 3.17547, 1.00185 and 0.86232 MHz, taken from Table S5. It is not possible to calculate for all of the HFCCs due to the computational time it would take. It is very clear that as soon as several proton HFCCs are included, the precession is heavily damped.

Spin exchange or reaction rate as a mechanism?

In the main manuscript, we have interpreted the light induced changes in the data to be due to a change in the reactivity of the muonium with the molecule. However, another possible mechanism that can explain the increased amplitude of the ALC for site 2 is electron spin exchange, whereby the spin of the electron associated with the muonium undergoes a spin exchange with the total spin of the excited state. Another possible mechanism might be the ground-state muoniated radical electron spin exchanging with a second excited molecule. Electron spin exchange, or electron spin relaxation, can account for a dramatic increase in ALC amplitude as has previously been shown for TIPS-Pn in the solid state[32]. We start by noting that in order for a particular model to be applicable, it must agree with all of the experimental data presented. It must be able to:

- Result in an increase, *and decrease*, in integral ALC amplitude;
- Account for the light induced changes to the low TF data;
- Account for the light induced changes to the time dependent data on resonance.

We start by attempting to obtain good agreement between the two models – electron spin exchange and muonium reaction rate. Figure S11a-c shows the ALC spectra for light on and off, with three different scenarios modelled, for both light on and light off data. The three models contain two overlapping ALCs. For the light-off data, the muon HFC constant of 200 MHz and 198.9 MHz was used for sites 1 and 2 respectively, and both sites were calculated with a proton HFC constant of 65 MHz. These are consistent with the HFC constants extracted from the DFT calculations. The scaling factors between polarization and asymmetry were then estimated for

the light off data, and then fixed for the light on data. We note that since we do not know the reaction rate constant for this solute/solvent combination, the scaling factor between polarization and asymmetry is arbitrary, but the ratio between light-on and light-off amplitudes can demonstrate the essential physics – whether electron spin exchange or chemical reaction rate. By fixing it to the light-off state, the three models for additional dynamics from the excitation are the only factors in determining the change in amplitude. In addition to the effect of electron spin exchange and a change in reaction rate, which are discussed below, in all cases in order to account for the light on data, the muon HFC constant for site 2 had to be reduced to 198.6 MHz, although a similar change to the proton HFC could have a similar effect. These values are summarized in Table S6. There were no other changes to either muon or proton HFC constant. The data in all cases were modelled using the Quantum programme[47]. The ALC spectra are readily modelled using this software, based on the time evolution of the muon spin ensemble via a spin density matrix formalism as summarized in ref [22]. The dynamic processes can be modeled by considering the situation as a dynamical exchange between two stationary states[51], with an exponential transition between these states. For example, a bi-directional electron spin flip rate or a chemical reaction rate via a uni-directional and permanent change in HFC constants. Further details can be found elsewhere in the literature.[22,47,50]

		Ground State		Excited State	
	Site	1	2	1	2
Model 1	A_μ (MHz)	200	198.9	200	198.6
	A_k (MHz)	65	65	65	65
	S_{er} (MHz)	0	0	0	0.3
Model 2	A_μ (MHz)	200	198.9	200	198.6
	A_k (MHz)	65	65	65	65
	K_R (MHz)	0.5	0.5	0.5	0.7
Model 3	A_μ (MHz)	200	198.9	200	198.6
	A_k (MHz)	65	65	65	65
	K_R (MHz)	2	2	2	2.9

Table S6: Summary of the different HFCCs, electron spin exchange rate (S_{er}) and reaction rate (K_R) for the three models used. In the case of the reaction rate, the initial state had an A_μ and A_k of 4463 and 0 MHz respectively and was 100% populated.

Figure S12a shows the affect that increasing the spin exchange rate on site 2 from 0, for the light-off data, to 0.3 MHz for the light-on data. Site 1 had its spin exchange rate fixed to 0 for both light on and off, which is reasonable given there no light induced change to the lineshape at the high field side. We note that this suggests a mechanism localized to a single ALC, a point that we shall return to shortly. Having an electron spin exchange rate of 0 when no excitation is present is reasonable given there is no excitation to exchange spin with, although it could be there are other spin relaxation processes present. However, any additional spin relaxation process will merely result in a non-zero ground state relaxation rate and a subsequent increase in the

relaxation rate when the excitation is present. A rate of 0 and 0.3 MHz represents the minimum spin exchange rate to account for the ALC spectra. Nonetheless, it is very clear that from Figure S12a that electron spin exchange *can* account for the increase in amplitude of the ALC.

Shown in Figures S12b and c are the calculated spectra for the model for reaction rate, in two different limits. In this case, the initial state (100% populated) had a muon HFCC of 4463 MHz and proton HFCC of 0. A uni-directional exponential transition to the muoniated radical state was then included, with the HFCCs summarized in Table S6. As can be seen from Table S6, the rate constant was larger for the light-on state only for site 2, and was unchanged for site 1.

We first discuss Figure S12b, where the muonium reaction rate for site 2 increases from 0.5 MHz for light off to 0.7 MHz for light on. Both light on and off are very good matches to the data. We chose 0.5 MHz as the initial rate constant, as this is reasonably well matched to the triplet precession lifetime in low transverse fields (Figure 3 of the main manuscript). However, we note that a portion of this triplet precession could be from muonium in the SiO_2 window of the sample cell, and the ~2 μs lifetime evident in Figure 3 may be dominated by them. Because of this uncertainty, we have modelled the lineshapes in a different reaction rate limit. Figure S11c compares a muonium reaction rate constant increasing from 2 MHz for light off to 2.9 MHz for light on, and shows an equally good match to the data as in Figure S12b, which is achieved by a change to the ground-state scaling factor between measured asymmetry and calculated polarisation.

We can therefore conclude that the effect of a change in reaction rate is indistinguishable from the introduction of spin exchange if one solely looks at the ALC amplitude. Nonetheless, we believe that electron spin exchange cannot account for the light induced changes to the ALCs. Firstly, electron spin exchange cannot account for the *reduction* in ALC amplitude observed at higher times (see Fig 2c), whereas a reduction in chemical reactivity can. Secondly, electron spin exchange is mediated via relatively long range interactions as a result of the delocalized unpaired electron and excitation wavefunctions. Moreover, we would expect the coupling to be large. Spin exchange or relaxation that is driven by the presence of the excitation should have some affect on *all* ALCs; this is not the case. However, to properly assess whether electron spin exchange or a modified reaction rate is relevant in this situation, as noted above, the mechanism must also be compatible with the low transverse field data and the on-resonance time dependent data.

Shown in Figures S12d-f are the simulated time spectra for light on and light off, calculated under the same conditions as the ALC spectra in Figures S12a-c, for a fixed field of 710 mT (corresponding to the largest light induced difference observed in the experimental ALC spectra). Firstly, we note that the oscillations are not observable in the data, either light on or off. This is most likely related to some additional relaxation processes being present in the real experiment that are not accounted for in our modelling, for example subtle variations in the HFC due to different conformations or a limited “tumbling” rate of this large molecule. Nonetheless, it is immediately clear that the spin exchange mechanism is a traditional relaxation phenomena, which would manifest itself in our data by an increase in relaxation rate when the excitation is present. Figures S12e-f show the time spectra for the model for reaction rate, where the situation is somewhat more complicated. In addition to there being a change in relaxation rate, it is evident that the precession amplitude increases upon increasing the reaction rate and changing the HFC. This is far more noticeable in the than for the spin exchange model. This would manifest itself as a linear shift in the data, as indicated by the schema in Figure S12f.

Shown in Figure S12g is the different between light-on and light-off data taken in our photomusr experiment at a fixed field of 710 mT, along with two fits. It is immediately clear that there is a significant *linear shift* of the data as indicated by the green line, with no immediately obvious change in relaxation rate. This is further demonstrated by Figure S12h, which shows the fitted relaxation rate across the field range of the ALC. Not only is there no increase in the relaxation rate as one scans through the ALC, there is no difference in the relaxation rate when the sample is illuminated. This strongly suggests that spin exchange, which would result in an increased relaxation rate, is not responsible for the light-induced changes demonstrated in the ALC spectra. Figures S12g and h demonstrate that the main mechanism responsible for the increased ALC amplitude is one that involves a linear shift. Moreover, we note that with a relaxation rate of approximately 0.03 μs^{-1}, this limits the maximum spin exchange rate to a similar value, which is *ten times smaller* than is needed to account for the light-induced changes to the ALC spectra.

Finally, one must account for the low transverse field data shown in Figure 3. Shown in Figures S12i-k are the time spectra for a small transverse field of 0.4 mT for the same three sets of parameters. Of most interest is the time spectra for spin exchange, shown in Figure S12i, where it is clear that there is very little change between a spin exchange rate of 0 and 0.3 MHz. Moreover, as a result of the three-spin system, the oscillations are a different frequency to those from the solvated muonium, and so wouldn't affect the fits to Figure 3. On the other hand, both of the reaction rate time spectra show significant differences that are commensurate with the experimental data.

We therefore conclude that both the time dependent data and the time integrated ALC data can only be explained via a reaction rate change, and whilst electron spin exchange can adequately explain the ALC spectra, it cannot be responsible for the light induced changes on this occasion.

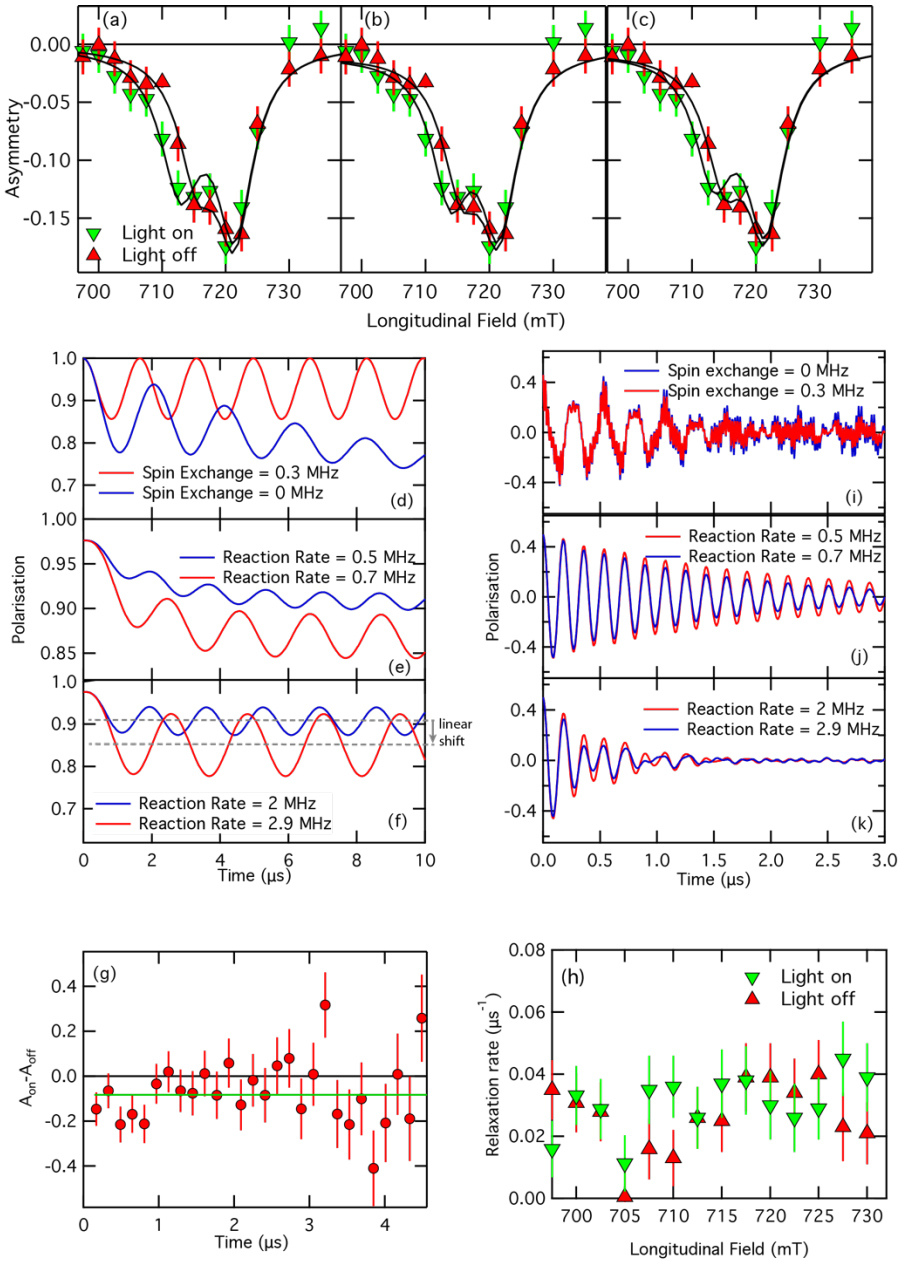

Figure S12: (a-c) ALC spectra for light-on and -off compared to three models – (a) electron spin exchange of 0 and 0.3 MHz, (b) a reaction rate of 0.5 and 0.7 MHz and (c) a reaction rate of 2 and 2.9 MHz for light off and light on, respectively. Panels (d-f) show the associated model time spectra for the same conditions, at a fixed field of 710 mT. Of note is the linear shift in (f). This is a way to differentiate between the models. Panel (g) shows the experimental difference between light on and off for 710 mT that has been an linear shift. Panel (h) shows the fitted exponential relaxation rate for light-on and -off as a function of applied field. No increase in relaxation rate is found across the ALC, and moreover, there is no difference between the light-on and -off data. Panels (i-k) show the modelled time spectra in a transverse field of 0.4 mT under the same conditions. Very little change in the first few μs can be seen for the spin exchange model (h), which is where the experimental data shows a difference, yet there is a change in both limits of the reaction rates (i,j) that is commensurate with the changes seen in the experimental data.

References:

42. M. Kaupp, M. Bühl, V. G. Malkin, *Calculation of NMR and EPR Parameters: Theory and Applications* (WILEY-VCH Verlag GmbH & Co. KGaA , 2004) p489-491.

43 K. Wang, L Schulz, M. Willis, S, Zhang, A. J. Misquitta, A. J. Drew, Spintronic and electronic phenomena in organic molecules measured with μSR. Accepted in *Jnl. Phys. Soc. Jap.* (2016)

44 43. S. Agostinelli *et al.*, Geant4—a simulation toolkit. *Nuclear Instruments and Methods in Physics Research Section A: Accelerators, Spectrometers, Detectors and Associated Equipment* **506**, 250 (2003).

45 K. Yokoyama et al., The new high field photoexcitation muon spectrometer at the ISIS pulsed neutron and muon source. Submitted to *Rev. Sci. Inst.* (2016); arXiv:1607.06145

46 P. Murahari et al., in preparation.

47. J. S. Lord, Computer simulation of muon spin evolution. *Physica B* **374-375**, 472-474 (2006).

48. D.A. Geeson et al., Evidence for a triple-bond muonium adduct. *Chem. Phys. Lett.* **116**, 186 (1985)

49. C.J. Rhodes et al., Muonium-containing vinyl radicals. *J. Chem. Soc. Chem. Commun.* 447, (1987)

50. S. Lord, S. F. J. Cox, M. Charlton, D. P. Van der Werf, R. L. Lichti, and A. Amato. The muon spin response to intermittent hyperfine interaction: modelling the high- temperature electrical activity of hydrogen in silicon. *J. Phys.: Cond. Matt.* **16**, S4739, (2004).